APPROXIMATING THREE-DIMENSIONAL FLUID FLOW IN A MICROFLUIDIC DEVICE WITH A TWO-DIMENSIONAL, DEPTH-AVERAGED LATTICE BOLTZMANN METHOD

BY

ARTIN LALEIAN

THESIS

Submitted in partial fulfillment of the requirements
for the degree of Master of Science in Environmental Engineering in Civil Engineering
in the Graduate College of the
University of Illinois at Urbana-Champaign, 2014

Urbana, Illinois

Advisers:

Professor Albert J. Valocchi
Professor Charles J. Werth

ABSTRACT

Microfluidic devices (MFDs) are important tools in the study of reactive transport processes in porous media. Laboratory and numerical experiments have studied reactions such as bimolecular complexation, biodegradation and biofilm growth, and mineral precipitation coupled to fluid flow in MFDs that are shallow rectangular channels with regular or irregular interior pore structure. The success of these reactive transport models is dependent on accurate determination of the velocity field, because reaction is coupled to solute transport. The small aspect ratio of these devices has led to their approximation as two-dimensional (2D) objects in numerical models. This approximation may neglect significant three-dimensional (3D) effects on the velocity field and contribute to model error. To avoid the computational cost of a 3D numerical model, some 3D effects may be approximated in a 2D model. In prior work in the literature, viscous drag from the top and bottom boundary surfaces omitted by the 2D simulation has been approximated and applied as an external body force acting on the fluid for the case of constant depth throughout the MFD. This work generalizes the approximation to cases of variable depth to account for the possibility of precipitate or biofilm formation along those surfaces omitted by the 2D simulation. The 2D lattice Boltzmann method (LBM) is reformulated to solve the depth-averaged Stokes equations and the viscous drag body force approximation is applied. The 2D, depth-averaged LBM is benchmarked by comparison to depth-averaged results of the 3D LBM in several test geometries. Excellent agreement is observed between the results of the two methods in contracting-expanding channel geometries. Agreement is not as favorable in more complex flows, such as flow around a cylinder or in a MFD unit cell. In addition, a comparison of run times demonstrates the reduction in computational cost with the 2D, depth-averaged LBM.

ACKNOWLEDGEMENTS

I would like to thank my graduate advisors, Professor Charles J. Werth and Professor Albert J. Valocchi, for their guidance in completing this work, as well as Dr. Haihu Liu for his help in answering questions along the way. In addition, I owe thanks to my family for their unrelenting support of my graduate studies. Part of this work was supported by the Department of Energy Environmental Remediation Science Program, under award numbers DE-SC0001280 and DE-SC0006771. This material is based upon work supported by the National Science Foundation Graduate Research Fellowship Program under Grant Number DGE-1144245.

TABLE OF CONTENTS

CHAPTER 1: INTRODUCTION

Pore-scale reactive transport processes, such as bimolecular complexation and carbonate mineral precipitation, have been studied with microfluidic devices (MFDs), model porous media with simple interior pore structure composed of silicon (Willingham et al. 2008, Zhang et al. 2010). Carbonate precipitation is of interest in carbon capture and storage (CCS) systems because precipitate buildup can reduce aquifer storage capacity by blocking pores, thereby reducing the aquifer's effective porosity. Understanding the dynamics of subsurface mineral precipitation is vital to predicting the success of CCS systems. MFD experiments have also been used to study other important processes such as biodegradation with biofilm growth (Nambi et al. 2003), and multiphase flow. Laboratory and numerical experiments with MFDs aim to characterize the complex dynamics involved in subsurface transport and reaction.

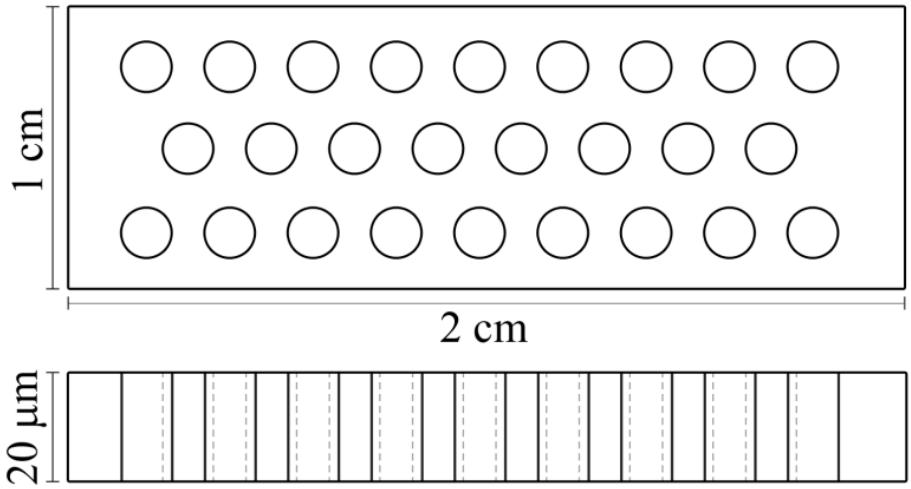

Figure 1: Top and side views of MFD. Lengths are not to scale. Actual MFD contains many more cylindrical pillars than depicted here.

The exterior geometry of a MFD is a shallow rectangular channel, with a cross-sectional depth to width ratio on the order of 10^{-3}, as depicted in Figure 1. Because the flow depth is small relative to the flow width, numerical models have approximated the MFD as a two-dimensional (2D) system by neglecting its depth and employing 2D numerical methods for solute transport and reaction (Willingham et al. 2008, Willingham et al. 2010). The primary motivator for reducing the MFD's physical dimensions is the accompanying reduction in computational cost of

the numerical model.

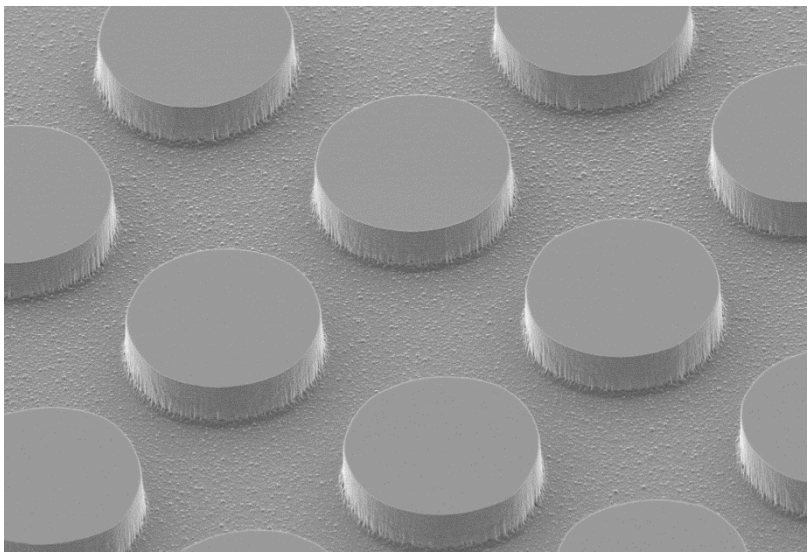

Figure 2: Scanning electron microscope image of cylindrical pillars in real MFD.

Still, the three-dimensional (3D) nature of the system cannot be completely ignored. The 2D model of Yoon et al. (2012) implicitly includes the MFD's depth by confining precipitate growth to the top and bottom surfaces of the MFD, which are not explicitly present in the 2D domain. In Figure 3, the centered horizontal line is the plane included in the simulation and the solid blocks are mineral precipitate, assumed to grow symmetrically above and below that plane. Their model tracks precipitate accumulation outside the plane, assuming complete blockage to flow when this amount exceeds a threshold value. Thus, the MFD's interior depth is both transient and spatially-variable as precipitate can grow and dissolve from the implicit top and bottom surfaces.

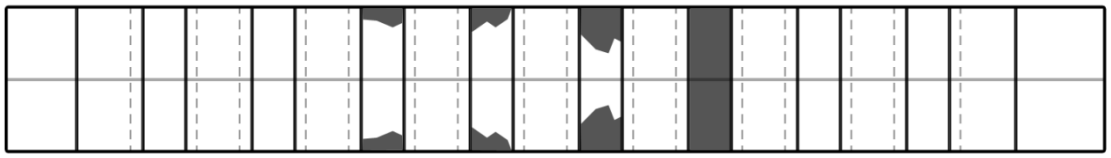

Figure 3: Magnified side view of MFD. The centered horizontal line represents the domain of the 2D simulation. Symmetric precipitate growth is shown from the top and bottom surfaces.

Neglecting a spatial dimension of the MFD results in model error due to 3D effects not captured in the 2D approximation. For example, the top and bottom surfaces impart viscous drag that reduces fluid speed, and local variation in depth redirects flow, e.g. away from highly-

blocked regions. Existing 2D models do not capture these effects. We propose an improved approach to determine a 2D velocity field in the MFD with a depth-averaged lattice Boltzmann method (LBM) that incorporates the 3D effects of viscous drag with depth variation.

To define a successful 2D representation of the depth-averaged true 3D velocity field, first assume a 3D velocity field is available, denoted $\boldsymbol{u_{3D}}(x, y, z) = \left[u_{3D,x}\ u_{3D,y}\ u_{3D,z}\right]^T$. It is a function of three spatial coordinates and may be obtained by the 3D LBM or other fluid flow solver. Its 2D representation is obtained by averaging across the MFD's depth, yielding three depth-averaged velocity components. After omitting the vertical component, the resulting 2D velocity field may be denoted $\bar{\boldsymbol{u}}_{\boldsymbol{3D}}(x, y) = \left[\bar{u}_{3D,x}\ \bar{u}_{3D,y}\right]^T$. For the purposes of this work, $\bar{\boldsymbol{u}}_{\boldsymbol{3D}}(x, y)$ is the desired solution for flow in the MFD. The middle column in the diagram below summarizes the process just described.

Flow diagram describing various approaches to solution

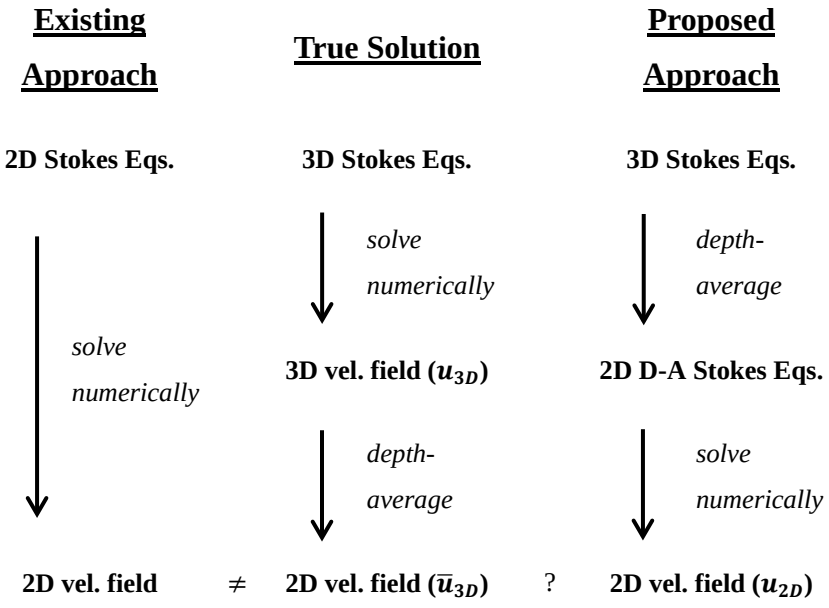

Our goal is to obtain $\bar{\boldsymbol{u}}_{\boldsymbol{3D}}$ while avoiding the computational cost of determining the 3D velocity field. The model of Yoon et al. (2012) determines the 2D velocity field by solving the 2D Stokes equations with the LBM (left column of the diagram). However, the resulting 2D

velocity field may not closely approximate $\bar{\boldsymbol{u}}_{\boldsymbol{3D}}$ in local velocity. As a simple example, transverse analytical velocity profiles are compared in Figure 4 for flow in an open, constant-depth 2D channel. Analytical velocity profiles, which will be discussed in more detail, are available in Appendix A. One velocity profile includes the 3D effect of viscous drag from the implicit top and bottom surfaces. The other profile does not include this effect, resulting in the characteristic parabolic profile of Poiseulle flow. Under identical pressure gradient and fluid viscosity, the two analytical profiles match neither in total flow rate nor in shape. The flow rate may be matched by scaling one velocity profile, but there could still be some error in local velocity.

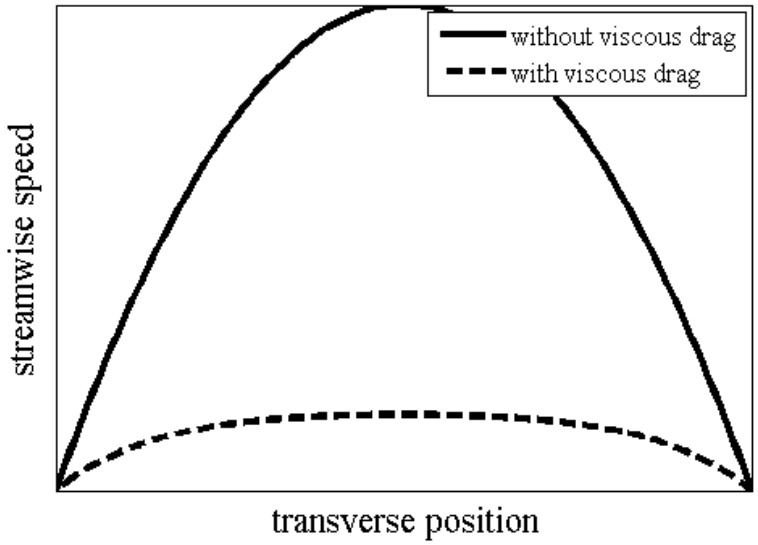

Figure 4: Transverse velocity profile in an open, constant-depth 2D channel, with and without viscous drag from implicit top and bottom surfaces. Without viscous drag is Poiseuille flow.

An alternative approach is summarized in the right column of the diagram. First, the 3D Stokes equations are depth-averaged, yielding three equations in three depth-averaged velocity components. The equation in the vertical component is omitted, leaving two governing equations to be solved numerically. The 2D LBM can be modified to solve these depth-averaged equations. Ideally, the resulting 2D velocity field, denoted $\boldsymbol{u}_{\boldsymbol{2D}}(x, y) = \left[u_{2D,x}\ u_{2D,y}\right]^T$, closely approximates $\bar{\boldsymbol{u}}_{\boldsymbol{3D}}$. If so, we have obtained an improved 2D velocity field without first

determining a 3D velocity field.

The reduction in computational cost relative to a 3D approach is not the only benefit of the proposed 2D approach. Note that in both a 2D and 3D model, precipitate may grow in such a way as to produce narrow constrictions to flow that are spanned by only a few fluid nodes. With fewer than four fluid nodes within such a constriction, the LBM is not expected to produce a realistic velocity field (Succi 2001). Thus, there is a limit on how narrow a constriction should be allowed in the model to maintain model accuracy. In a 3D model, without confining precipitate growth to any surfaces, a narrow constriction would be problematic across the width or depth of the MFD. In a 2D model with implicit depth, only narrow constrictions across the width would be problematic.

Second, note that precipitate growth and dissolution is represented in a 3D model by changing the state of a node between solid and fluid. Thus, precipitation and dissolution only occur in discrete quantities, namely integer multiples of the node spacing, Δx. With the 2D approach the implicit MFD depth can take any real value greater than zero, meaning precipitation and dissolution can occur continuously. This is an improvement over the 3D method, because precipitate growth and dissolution are not constrained by the lattice in the vertical direction. Still, the horizontal position of precipitate is confined to nodes in the 2D domain.

CHAPTER 2: THEORETICAL BACKGROUND

2.1 The Lattice Boltzmann Method (LBM)

2.1.1 Choice of Lattice

The LBM is a mesoscopic numerical method for fluid simulation on a regular lattice in one, two, or three spatial dimensions. Each lattice node is connected to a subset (possibly all) neighboring nodes via lattice vectors, denoted $\boldsymbol{e_i}$. In the following text, vector symbols will appear in bold font and scalars in plain font. The set of lattice vectors defines all possible fluid particle velocities, requiring that particles remain on the lattice. When implementing the LBM, the choice of lattice and its connectivity depend on the spatial dimensions of the problem at hand and the available computational resources. Common lattice nomenclature takes the following form.

D (number of spatial dimensions) Q (lattice connectivity)

In the above expression, the number of spatial dimensions is most often two or three and the lattice connectivity is the size of the set of lattice vectors. D2Q9 and D3Q15 lattices are often encountered in the literature, and will be implemented in this work. Lattice vectors, $\boldsymbol{e_i}$, for the D2Q9 and D3Q15 lattices, indexed $i = 0, 1, \ldots, 8$ and $i = 0, 1, \ldots, 14$, respectively, are defined below for a unit lattice, with visual depictions in Figure 5 and Figure 6.

$i =$	0	1	2	3	4	5	6	7	8
$e_x =$	0	1	0	-1	0	1	-1	-1	1
$e_y =$	0	0	1	0	-1	1	1	-1	-1

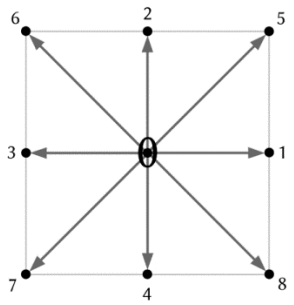

Figure 5: D2Q9 lattice vectors.

$i =$	0	1	2	3	4	5	6	7	8	9	10	11	12	13	14
$e_x =$	0	1	−1	0	0	0	0	1	−1	1	−1	1	−1	1	−1
$e_y =$	0	0	0	1	−1	0	0	1	−1	1	−1	−1	1	−1	1
$e_z =$	0	0	0	0	0	1	−1	1	−1	−1	1	1	−1	−1	1

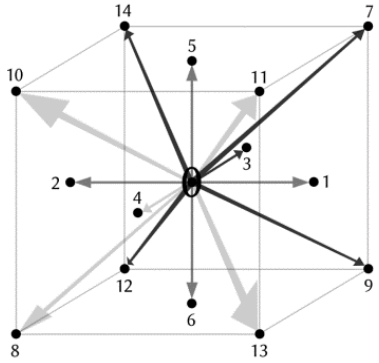

Figure 6: D3Q15 lattice vectors.

2.1.2 Macroscopic Fluid Quantities

The local fluid quantities of density and velocity are defined on each fluid node in terms of a set of scalars, denoted f_i, equal in number to the lattice vectors and indexed identically, which represent a collection of fluid particles (Sukop and Thorne 2007, Succi 2001). Each scalar in the set corresponds to a single lattice vector, including the zero vector that represents fluid particles at rest. These scalars originate from a probability distribution function (DF), and may be visualized as vectors by multiplication with their corresponding lattice vector. DF values may be interpreted physically as directional densities (Sukop and Thorne 2007), i.e. the fraction of all fluid particles at a lattice node which move in the direction of their corresponding lattice vector. This interpretation of DF values leads naturally to the definition of local fluid density, ρ, in Eq. 1 where $\boldsymbol{x}$ is the position vector of a lattice node. Time dependence is omitted, although all local quantities generally vary throughout the course of a LBM simulation.

$$\rho(\boldsymbol{x}) = \sum_i f_i(\boldsymbol{x}) \qquad \text{Eq. 1}$$

Local fluid momentum is a weighted sum of lattice vectors, the weights being DF values. Extending the previous physical interpretation, terms in the summation below may be considered directional momenta, their sum yielding the local net momentum.

$$\rho \boldsymbol{u} = \sum_i f_i \boldsymbol{e_i} \qquad \text{Eq. 2}$$

Pressure and density are related by the equation of state for an ideal gas, where c_s is the speed of sound on the lattice, a constant for all lattices implemented in this work.

$$P = \rho c_s^2 \qquad\qquad c_s = \frac{1}{\sqrt{3}}$$

Fluid kinematic viscosity is a function of a parameter τ, related to the interaction of fluid particles, as described shortly. In the equation below, Δt is the lattice time step, most often given a value of one (Sukop and Thorne 2007).

$$\nu = c_s^2 \left(\tau - \frac{\Delta t}{2}\right) \qquad \text{Eq. 3}$$

2.1.3 The Lattice Boltzmann Algorithm

The LBM proceeds in two sequential fundamental steps named streaming and collision. Each step may be understood from its purpose in lattice gas cellular automata (LGCA) models, a predecessor of the LBM that simulates a fluid with single particles on a regular lattice. In LGCA, streaming consists of propagating single particles one lattice node in their given direction of travel, or simply free motion of particles. Collision, as the name implies, involves accounting for interparticle collisions at each lattice node in such a way as to conserve local mass and momentum. The earliest LGCA models allowed only head-on collisions between two particles, which reversed their direction of travel, while later models considered additional possibilities. Streaming and collision are stated mathematically by the first and second equations below, respectively. The right-hand side (RHS) of the second equation is written in operator notation,

where Ω denotes the collision operator.

$$\text{Streaming:} \quad f_i(\boldsymbol{x} + \boldsymbol{e_i}\Delta t, t + \Delta t) = f_i(\boldsymbol{x}, t + \Delta t)$$

$$\text{Collision:} \quad f_i(\boldsymbol{x}, t + \Delta t) = \Omega[f_i(\boldsymbol{x}, t)]$$

In the LBM, streaming consists of free motion of DF values, in which they are propagated by one lattice node in the direction of their respective lattice vector. The LBM does not stream single particles, but a collection of particles represented by a DF value. As in the LGCA, collision in the LBM consists of accounting for local interparticle interactions. It is not immediately clear how to account for collision with DF values as opposed to single particles. As with LGCA, mass and momentum should be conserved in the LBM collision. The most common solution to this problem represents collision as a relaxation of DF values toward a local equilibrium, known as the BGK operator after its original authors (Bhatnagar et al. 1954). Local equilibrium is defined as a second-order Taylor expansion of the Maxwell distribution, shown in Eq. 4. Although not explicitly shown, both ρ and $\boldsymbol{u}$ are local quantities, $\rho = \rho(\boldsymbol{x})$ and $\boldsymbol{u} = \boldsymbol{u}(\boldsymbol{x})$. w_i are directional weights, which may be interpreted as variable particle masses across different lattice directions (Succi 2001). Values of w_i for the D2Q9 and D3Q15 lattices are shown below.

$$f_i^{eq}(\rho, \boldsymbol{u}) = w_i \rho \left[1 + 3(\boldsymbol{e_i} \cdot \boldsymbol{u}) + \frac{9}{2}(\boldsymbol{e_i} \cdot \boldsymbol{u})^2 - \frac{3}{2}(\boldsymbol{u} \cdot \boldsymbol{u})\right] \qquad \text{Eq. 4}$$

D2Q9

$$w_i = \begin{cases} 4/9 & i = 0 \\ 1/9 & i = 1-4 \\ 1/36 & i = 5-8 \end{cases}$$

D3Q15

$$w_i = \begin{cases} 2/9 & i = 0 \\ 1/9 & i = 1-6 \\ 1/72 & i = 7-14 \end{cases}$$

Relaxation toward local equilibrium means that during collision, f_i are shifted toward f_i^{eq} at a rate given by the relaxation parameter, τ. The BGK collision operator is expressed explicitly below.

$$\Omega[f_i(\boldsymbol{x}, t)] = f_i(\boldsymbol{x}, t) - \frac{f_i(\boldsymbol{x}, t) - f_i^{eq}(\rho, \boldsymbol{u})}{\tau}$$

The streaming and collision equations are now combined, with the BGK collision

operator included.

$$f_i(\boldsymbol{x} + \boldsymbol{e_i}\Delta t, t + \Delta t) = f_i(\boldsymbol{x}, t) - \frac{f_i(\boldsymbol{x}, t) - f_i^{eq}(\rho, \boldsymbol{u})}{\tau} \quad \text{Eq. 5}$$

2.2 The Incompressible Lattice Boltzmann Formulation

The LBM implementation described above (hereby referred to as the standard LBM) recovers the compressible Navier-Stokes (N-S) equations to second-order accuracy. Many applications aim to simulate incompressible flow, however, and an alternative formulation of the LBM is available (He and Luo 1997) which significantly reduces compressibility error. Under the new formulation, the same process which recovered the compressible N-S equations to second-order accuracy now recovers the incompressible N-S equations. Under the incompressible formulation, local density is calculated as in Eq. 1. Velocity, however, is calculated as momentum was in Eq. 2.

$$\boldsymbol{u} = \sum_i f_i \boldsymbol{e_i} \quad \text{Eq. 6}$$

The equilibrium distribution function also differs from Eq. 4, and is expressed in Eq. 7. As before, $\rho = \rho(\boldsymbol{x})$ and $\boldsymbol{u} = \boldsymbol{u}(\boldsymbol{x})$.

$$f_i^{eq}(\rho, \boldsymbol{u}) = w_i \left[\rho + 3(\boldsymbol{e_i} \cdot \boldsymbol{u}) + \frac{9}{2}(\boldsymbol{e_i} \cdot \boldsymbol{u})^2 - \frac{3}{2}(\boldsymbol{u} \cdot \boldsymbol{u})\right] \quad \text{Eq. 7}$$

2.3 Representation of Viscous Drag from Top and Bottom Surfaces

To characterize the viscous drag caused by the top and bottom surfaces of the MFD, first consider flow in a 3D constant-depth rectangular channel. This is the outer shell of a MFD, with no interior pore structure. Because the top and bottom surfaces are outside the 2D domain (refer to Figure 3), the viscous drag they impart on the fluid has to be accounted for artificially. The

analytical solution in Eq. 14 provides insight into the velocity profile's shape across the channel depth, away from the side walls. Figure 7 plots vertical sections of Eq. 14 taken at the transverse center ($y = 0$) of the channel cross section for varying aspect ratio (AR), the ratio of channel depth to width. For each AR, the profile is compared to a Poiseuille profile (Eq. 16) with equivalent pressure gradient and viscosity. With decreasing aspect ratio, the two profiles agree very well.

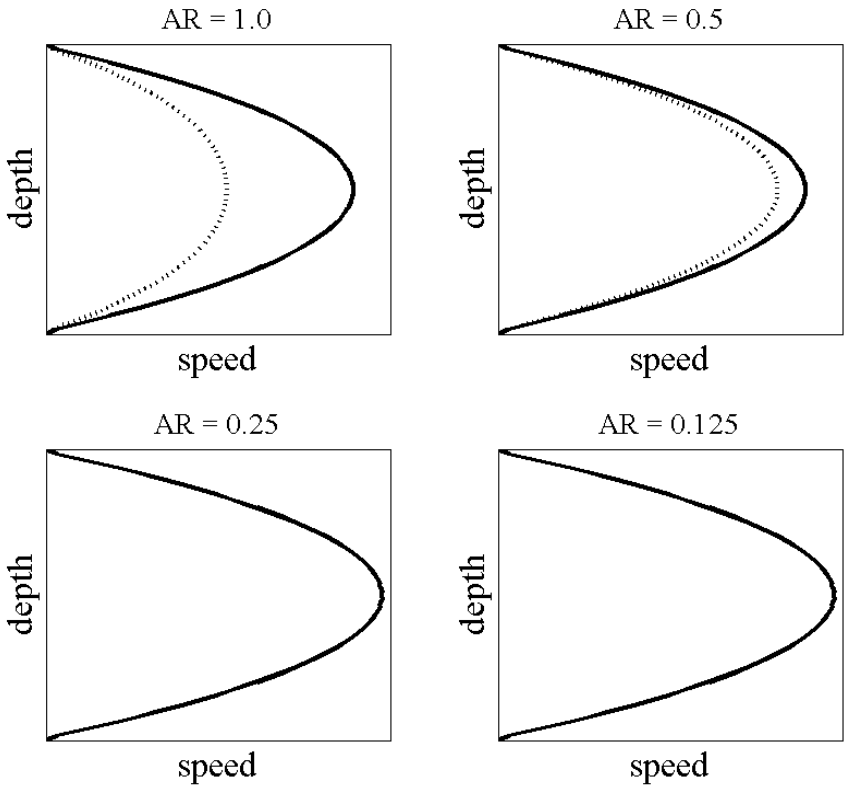

Figure 7: Central vertical cross sections of the 3D analytical velocity profile (dashed lines) with varying channel aspect ratio (AR), approximated with a parabolic profile (solid lines). Units are arbitrary.

Based on this evidence, we assume the velocity profile is exactly parabolic and therefore described by Eq. 16 for the small aspect ratio MFD geometries under consideration. Depth-averaging Eq. 16 yields its average value (u_{ave}). The pressure gradient, the driving force required to achieve the parabolic profile, may be expressed as a function of u_{ave}. Because the 3D velocity field will be depth-averaged to obtain $\overline{\boldsymbol{u}}_{\boldsymbol{3D}}(x, y)$, this is precisely the driving force of interest. In opposition is the resistive force imparted by the solid surfaces of the channel. At steady state

these forces are balanced, meaning the resistive viscous drag is equal in magnitude and opposite in direction of the driving pressure gradient. Any contribution of drag from the side walls is neglected. Replacing u_{ave} with the 2D LBM velocity, $\boldsymbol{u_{2D}}$, and dividing by ρ provides an expression for the acceleration due to viscous drag from the top and bottom surfaces.

$$
\begin{aligned}
u_{ave} &= \left(-\frac{dP}{dx}\right)\frac{h^2}{12\mu} \\
\frac{dP}{dx} &= -\frac{12\mu}{h^2}u_{ave} \\
\rho a_x &= -\frac{12\mu}{h^2}u_{ave} \\
a_x &= -\frac{12\nu}{h^2}u_{ave} \\
\boldsymbol{a_{drag}} &= -\frac{12\nu}{h^2}\boldsymbol{u_{2D}}
\end{aligned}
\qquad \text{Eq. 8}
$$

An expression similar to $\boldsymbol{a_{drag}}$ (using the maximum rather than average of the Poiseuille profile) was derived by Flekkoy et al. (1995) for the purpose of representing viscous drag in a Hele-Shaw cell, and applied to a constant-depth MFD by Venturoli and Boek (2006). Eq. 8 has been used by Boek and Venturoli (2010), also in a constant-depth channel.

2.4 Body Force Implementation

An external force may be included in the 2D LBM with an additional term in the collision step, with the form of F_i varying by implementation.

$$f_i(\boldsymbol{x} + \boldsymbol{e_i}\Delta t, t + \Delta t) = f_i(\boldsymbol{x}, t) - \frac{f_i(\boldsymbol{x}, t) - f_i^{eq}(\rho, \boldsymbol{u})}{\tau} + F_i\Delta t$$

In addition, some implementations shift the velocity field (Guo et al. 2002). Although some implementations have theoretical advantages over others, in practice there is little

difference between the numerical results obtained across implementations (Mohamad and Kuzmin 2010). For this reason, we utilize the relatively simple implementation of Luo (2000), where F_i takes the general form in Eq. 9, with $\boldsymbol{a}$ being the acceleration due to external forcing.

$$F_i = -3w_i\rho(\boldsymbol{e_i} \cdot \boldsymbol{a}) \qquad \text{Eq. 9}$$

2.5 Depth-Averaged Lattice Boltzmann Formulation

For incompressible Stokes flow, the governing continuum equations are the continuity and Stokes equations, where $\boldsymbol{u} = \boldsymbol{u}(x, y, z)$.

$$\nabla \boldsymbol{u} = 0$$
$$\mu \nabla^2 \boldsymbol{u} - \nabla P = 0$$

The standard 2D LBM will solve the 2D counterparts of the above equations. We first present an incomplete derivation of the depth-averaged continuum equations, then discuss the modifications needed for the 2D LBM to solve these equations. Let $\boldsymbol{u}(x, y, z) = \begin{bmatrix} u_x & u_y & u_z \end{bmatrix}^T$ and $h = h(x, y)$, the spatially-variable depth . The derivation below considers only the continuity equation, but may be applied to the momentum equation as well. First, the equation is depth-averaged.

$$\frac{1}{h}\left[\int_0^h \frac{\partial u_x}{\partial x} dz + \int_0^h \frac{\partial u_y}{\partial y} dz + \int_0^h \frac{\partial u_z}{\partial z} dz\right] = 0$$

Multiply by h, evaluate the last term, and reverse operator order for the first two terms:

$$\frac{\partial}{\partial x}\int_0^h u_x \, dz + \frac{\partial}{\partial y}\int_0^h u_y \, dz + u_z(x, y, h) - u_z(x, y, 0) = 0$$

With solid surfaces at $z = 0$ and $z = h$, i.e. the top and bottom walls, the vertical component of flow must be 0, leaving:

$$\frac{\partial}{\partial x}\int_0^h u_x \, dz + \frac{\partial}{\partial y}\int_0^h u_y \, dz = 0$$

The integrals describe component flow rates across the depth, which are equivalent to the depth-averaged velocity component multiplied by depth.

$$\frac{\partial(\bar{u}_x h)}{\partial x} + \frac{\partial(\bar{u}_y h)}{\partial y} = 0$$

$$\nabla(\bar{\boldsymbol{u}} h) = 0$$

$$\bar{\boldsymbol{u}} = \left[\bar{u}_x \;\; \bar{u}_y\right]^T$$

Similarly, the Stokes equations, with drag term now included, transform as below.

$$\nabla(\bar{p}h) = \mu\nabla^2(\bar{\boldsymbol{u}}h) - \frac{12\mu}{h^2}(\bar{\boldsymbol{u}}h)$$

Note that if h is constant, the depth-averaged equations reduce to the standard 2D continuum equations plus the viscous drag term. The depth-averaged equations differ from the standard 2D governing equations with viscous drag term only by the substitution $\boldsymbol{u} \rightarrow \bar{\boldsymbol{u}}h$. The same substitution is used to reformulate the incompressible 2D LBM so that it solves the depth-averaged governing equations. Local macroscopic velocity (Eq. 6) and the equilibrium distribution function (Eq. 7) of the incompressible 2D LBM are redefined in Eq. 10 and Eq. 11.

$$\boldsymbol{u}(x,y) = \frac{1}{h(x,y)}\sum_i f_i \boldsymbol{e_i} \qquad \text{Eq. 10}$$

$$f_i^{eq}(\rho, \boldsymbol{u}, h) = w_i\left[\rho + 3\mathrm{h}(\boldsymbol{e_i}\cdot\boldsymbol{u}) + \frac{9\mathrm{h}^2}{2}(\boldsymbol{e_i}\cdot\boldsymbol{u})^2 - \frac{3\mathrm{h}^2}{2}(\boldsymbol{u}\cdot\boldsymbol{u})\right] \qquad \text{Eq. 11}$$

2.6 Boundary Conditions

2.6.1 Periodic

Periodic boundaries connect two ends of the computational lattice by treating their nodes as adjacent to one another. The implementation requires no special treatment beyond the streaming process, which should propagate DF values between opposite boundaries.

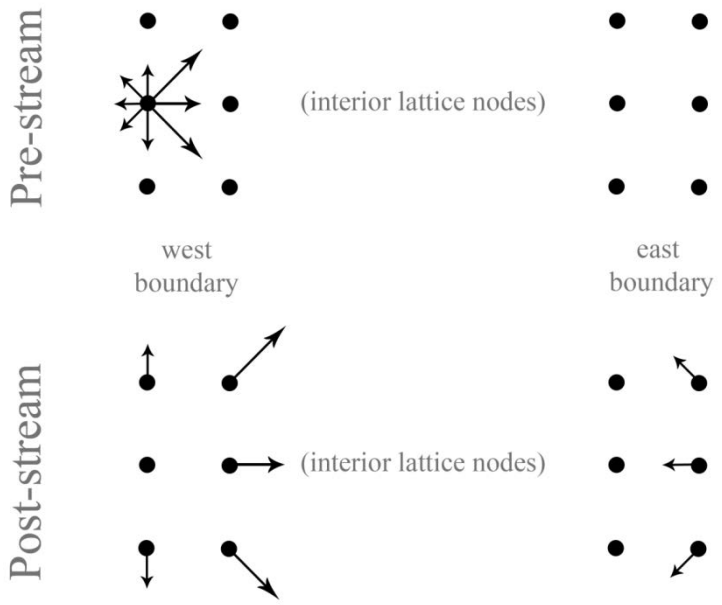

Figure 8: Schematic of streaming at an east-west periodic boundary node. Lattice extends beyond the nodes shown, both vertically and horizontally. DF values pointing out of the domain on the west boundary node stream to the east boundary.

2.6.2 No-slip

A great strength of the LBM for applications in porous media is its straightforward handling of complex solid-fluid boundaries. Each lattice node may be labeled as either solid or fluid and a localized boundary condition implemented to satisfy the no-slip condition. In this way the LBM can theoretically handle solid-fluid boundaries of arbitrary complexity. The most simple no-slip implementation is the halfway bounceback boundary condition. Any DF value which streams on to a solid node is reflected about the solid node so that it returns to its originating fluid node in the next iteration of streaming (Sukop and Thorne 2007). The halfway bounceback boundary effectively places the solid wall halfway between adjacent solid and fluid nodes, a fact that should be accounted for when representing physical lengths with the lattice.

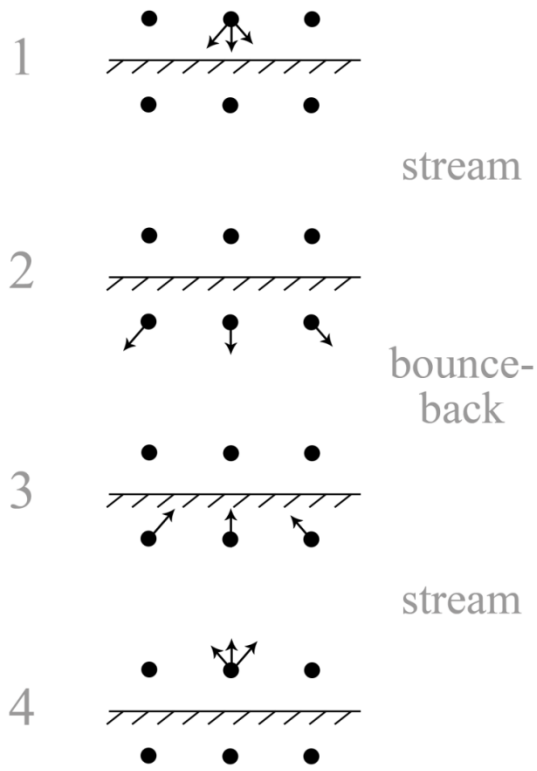

Figure 9: The halfway bounceback boundary condition. DF values pointing toward a wall stream onto solid nodes, are reflected, then stream back in the next iteration of the LBM. Effective wall position is halfway between adjacent solid and fluid nodes.

2.7 Unit Conversion

Most lattice Boltzmann implementations assign a value of one to both the node step Δx and time step Δt in lattice units. The former was implied by the lattice vectors $\boldsymbol{e_i}$ defined earlier.

$$\Delta x_l = \quad 1\ node\ step$$
$$\Delta t_l = \quad 1\ time\ step$$

Subscripts of l and p will denote lattice and physical units, respectively. Conversion between the two systems of units is possible, and will be used to refine the lattice in physical units while maintaining the values of Δx_l and Δt_l above. The general approach will be to define a physical system, convert it to a lattice system, determine a velocity field in lattice units, then

convert it to a velocity field in physical units. Suppose conversion factors for length and time have been specified in centimeters and seconds.

$$\Delta x_p \quad \frac{cm}{node\ step}$$

$$\Delta t_p \quad \frac{sec}{time\ step}$$

Any quantity involving length and time may be converted from a physical value to a lattice value. Conversion of velocity and kinematic viscosity are shown below, with units included in brackets.

$$u_l = u_p \left[\frac{cm}{sec}\right] \times \frac{1}{\Delta x_p}\left[\frac{node\ step}{cm}\right] \times \Delta t_p \left[\frac{sec}{time\ step}\right]$$

$$u_l = u_p \frac{\Delta t_p}{\Delta x_p}$$

$$\nu_l = \nu_p \left[\frac{cm^2}{sec}\right] \times \frac{1}{\Delta x_p^2}\left[\frac{node\ step}{cm}\right]^2 \times \Delta t_p \left[\frac{sec}{time\ step}\right]$$

$$\nu_l = \nu_p \frac{\Delta t_p}{\Delta x_p^2}$$

In principle, both Δx and Δt may be chosen freely. Δx is selected to result in adequate resolution of the physical system. A good rule of thumb for selecting Δt is to scale it with Δx by the relation $\Delta t \sim \Delta x^2$, which derives from the requirement that compressibility error and discretization error are the same order of magnitude (Latt 2008). We use the relation $\Delta t = 5\Delta x^2$.

CHAPTER 3: METHODS

3.1 Lattice Boltzmann Code

The LBM in 2D and 3D is implemented in a custom Fortran code. In both 2D and 3D, the code implements the incompressible formulation with an external body force. In the 2D method, the body force consists of both a driving acceleration (i.e. pressure gradient) and a resistive acceleration (i.e. viscous drag). In the 3D method, the body force consists of only a driving acceleration. For standard LBM subroutines, see Sukop and Thorne (2007).

3.2 Depth-averaging the 3D Velocity Field

Although three components of the 3D velocity field $\boldsymbol{u_{3D}}(x, y, z)$ may be depth-averaged, only the streamwise ($u_{3D,x}$) and transverse ($u_{3D,y}$) components, i.e. those components parallel to the horizontal plane, can be compared against $\boldsymbol{u_{2D}}(x, y)$. Thus, the vertical component of the depth-averaged 3D velocity field is omitted in $\overline{\boldsymbol{u}}_{\boldsymbol{3D}}(x, y)$.

$$\overline{\boldsymbol{u}}_{\boldsymbol{3D}}(x, y) = \frac{1}{h(x, y)} \int_0^{h(x,y)} \boldsymbol{u_{3D}}(x, y, z)\ dz$$

Numerical integration is performed using the composite trapezoidal approximation, shown below for a series of $n + 1$ equally-spaced points. The x and y coordinates are indexed because integration is performed independently at each node in the horizontal plane. u in the equation below refers to a single component of velocity.

$$\int_a^b u(x_i, y_i, z)\ dz \approx \left(\frac{h(x_i, y_i)}{2n}\right) [u(x_i, y_i, z_1) + 2u(x_i, y_i, z_2) + \cdots + 2u(x_i, y_i, z_n) + u(x_i, y_i, z_{n+1})]$$

3.3 Velocity Field Convergence

The LBM is iterated to steady-state, at which time simulated velocities fields are compared. The velocity field is considered steady when the inequality below (Zou and He 1997) is satisfied. Summations are evaluated over the entire lattice. The superscript * denotes the velocity field may be either $\boldsymbol{u_{3D}}(x, y, z)$ or $\boldsymbol{u_{2D}}(x, y)$.

$$\sqrt{\frac{\sum \|\boldsymbol{u}^*(t) - \boldsymbol{u}^*(t-1)\|^2}{\sum \|\boldsymbol{u}^*(t)\|^2}} < 10^{-6}$$

3.4 Geometric Parameters

The entire MFD is not simulated due to computational limitations. Rather, the dimensions of a representative unit cell are used to define the numerical lattice size. In the numerical experiments to follow, the interior geometry will often differ from that shown in Figure 10, but the exterior dimensions will not. The length, width, and depth of the 3D unit cell are 335, 335, and 20 μm, respectively. These physical lengths are denoted $l, w,$ and h. Note the 2D domain for simulation has explicit dimensions of l, w and an implicit dimension h, which may be spatially-variable. Lattice node spacing should be selected to adequately resolve the cell's depth, with no less than four fluid nodes spanning the channel depth in order to produce realistic results (Succi 2001). Recall this is a consideration for the 3D simulation, where the cell's depth is explicitly defined. After defining the node spacing, the lattice dimensions, i.e. the number of nodes in each dimension, are calculated as follows.

$$n_x = \frac{l}{\Delta x} + 1 \qquad n_y = \frac{w}{\Delta x} + 1 \qquad n_z = \frac{h}{\Delta x} + 1$$

The expressions above should be modified by adding a value of one if halfway bounceback boundaries are implemented, because they effectively place the solid wall halfway between adjacent fluid and solid nodes. The loss of length $\Delta x/2$ near each wall is balanced by addition of an extra node, thereby adding a length of Δx to the dimension containing two halfway bounceback boundaries.

In all simulations except those for LBM code benchmarking, Δx is given a value of 1.25 μm, yielding $n_x = 269$, $n_y = 269$, and $n_z = 18$. In the benchmarking case, the node spacing is varied such that $\Delta x = \{5.0,\ 2.5,\ 1.25,\ 0.625\}\ \mu m$.

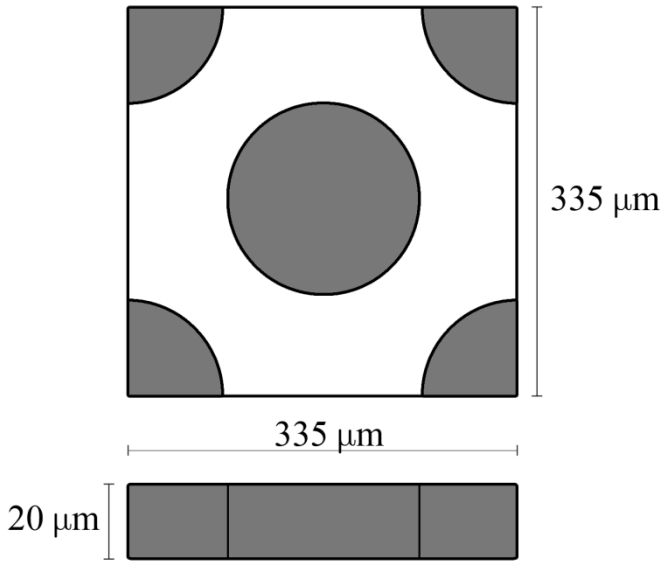

Figure 10: Unit cell geometry for the MFD, with cylindrical pillars. Depth is exaggerated. All boundaries are periodic.

3.5 Fluid Parameters

To compare $\boldsymbol{u_{2D}}(x, y)$ and $\overline{\boldsymbol{u}}_{\boldsymbol{3D}}(x, y)$, we wish to obtain equivalent flow rate in both simulations. For open channels, this is done by utilizing the analytical velocity profiles in Eq. 14 and Eq. 18. Suppose a target average velocity u_{ave} and fluid dynamic viscosity, μ, are specified for the physical system. Then we may calculate the pressure gradient that should drive flow as a function of these specified values. For the 3D simulation, the pressure gradient is given by Eq. 12, derived by rearranging Eq. 14. For the 2D simulation, it is given by Eq. 13, derived in Appendix C.

$$\frac{dP}{dx} = \frac{3u_{ave}\mu}{a^2}\left[\frac{192w}{\pi^5 h}\sum_{i=1,3,\ldots}^{\infty}\left(\frac{\tanh\left(\frac{i\pi h}{2w}\right)}{i^5}\right) - 1\right]^{-1} \quad \text{Eq. 12}$$

$$\frac{dP}{dx} = \frac{6k_1 w u_{ave}\mu}{h^2}\left[\frac{(1-k_2)e^{k_2} - (1+k_2)e^{-k_2}}{e^{k_2} + e^{-k_2}}\right]^{-1} \quad \text{Eq. 13}$$

$$k_1 = \frac{2\sqrt{3}}{h} \qquad k_2 = \frac{k_1 w}{2}$$

Pressure gradients are represented in the simulation as a constant body force driving flow, necessitating their expression as an acceleration, a_x, for the implementation in Eq. 9. Newton's second law of motion relates the pressure gradient and acceleration. Because fluid density, ρ, is given a value of 1.0 in lattice units, the acceleration and pressure gradient are equivalent in the simulation. Still, it is necessary to convert the pressure gradient from physical to lattice units as shown earlier.

$$F_x = \frac{dP}{dx}V = ma_x$$

$$\frac{dP}{dx} = \rho a_x$$

$$a_x = \frac{1}{\rho}\frac{dP}{dx}$$

For cases of variable-depth geometry, the method differs from that of the constant-depth channel. In particular, it is not known a priori how to specify the pressure gradients in 2D and 3D such that the same volumetric flow rate is obtained in $\boldsymbol{u_{2D}}(x,y)$ and $\overline{\boldsymbol{u}}_{\boldsymbol{3D}}(x,y)$. Therefore, 2D and 3D flow is driven with the same pressure gradient. After convergence, $\boldsymbol{u_{2D}}(x,y)$ is scaled uniformly such that its volumetric flow rate at the inlet is equal to that of $\overline{\boldsymbol{u}}_{\boldsymbol{3D}}(x,y)$ at the inlet. The scale factor is the ratio of the two flow rates, as shown below. Inlet flow rates are determined by numerically evaluating the integrals below with the composite trapezoidal approximation.

$$Q_{\boldsymbol{u_{2D}},in} = \int_{in} u_{2D,x}\,(0,y)\,dy$$

$$\left(\frac{Q_{\bar{\boldsymbol{u}}_{\boldsymbol{3D}},in}}{Q_{\boldsymbol{u_{2D}},in}}\right) Q_{\boldsymbol{u_{2D}},in} = \left(\frac{Q_{\bar{\boldsymbol{u}}_{\boldsymbol{3D}},in}}{Q_{\boldsymbol{u_{2D}},in}}\right) \int_{in} u_{2D,x}\,(0,y)\,dy$$

$$Q_{\bar{\boldsymbol{u}}_{\boldsymbol{3D}},in} = \int_{in} \left(\frac{Q_{\bar{\boldsymbol{u}}_{\boldsymbol{3D}},in}}{Q_{\boldsymbol{u_{2D}},in}}\right) u_{2D,x}\,(0,y)\,dy$$

$$Q_{\bar{\boldsymbol{u}}_{\boldsymbol{3D}},in} = \int_{in} \bar{u}_{3D,x}\,(0,y)\,dy$$

Scaling is justified by linearity of the governing equations, the steady-state Stokes equations. Because any scaling of the pressure gradient will scale the velocity field identically, scaling the velocity field following convergence is equivalent to scaling the pressure gradient prior to simulation.

3.6 Boundary Conditions

The inlet and outlet boundaries, i.e. the planes $x = \pm l/2$ are periodic in all simulations. The side boundaries, planes $y = \pm w/2$, are also periodic in all simulations except for the purposes of benchmarking the flow code, where they are no-slip boundaries, as required by the analytical velocity profiles. The top and bottom boundaries, planes $z = \pm h/2$, are no-slip in all cases.

3.7 Error Calculation

Error in $\boldsymbol{u_{2D}}(x,y)$ is calculated relative to $\bar{\boldsymbol{u}}_{\boldsymbol{3D}}(x,y)$. Reported errors will be for the maximum value of one component of $\boldsymbol{u_{2D}}(x,y)$ or $\bar{\boldsymbol{u}}_{\boldsymbol{3D}}(x,y)$ across all fluid nodes,

denoted $\max u_i^*$, or the average value of one component across all fluid nodes, denoted $\langle u_i^* \rangle$. In the equations below, $i = x$ represents the streamwise component and $i = y$ represents the transverse component.

$$E_i = \frac{\max u_{2D,i} - \max \bar{u}_{3D,i}}{\max \bar{u}_{3D,i}} \times 100\%$$

$$E_i = \frac{\langle u_{2D,i} \rangle - \langle \bar{u}_{3D,i} \rangle}{\langle \bar{u}_{3D,i} \rangle} \times 100\%$$

CHAPTER 4: RESULTS

4.1 Benchmarking the LBM Fortran Code

The Fortran code used in all simulations is benchmarked by comparison of the simulated velocity field to the analytical velocity profiles in Eq. 14 and Eq. 18. The open channel geometry is shown in Figure 11. All boundaries except the inlet and outlet are no-slip.

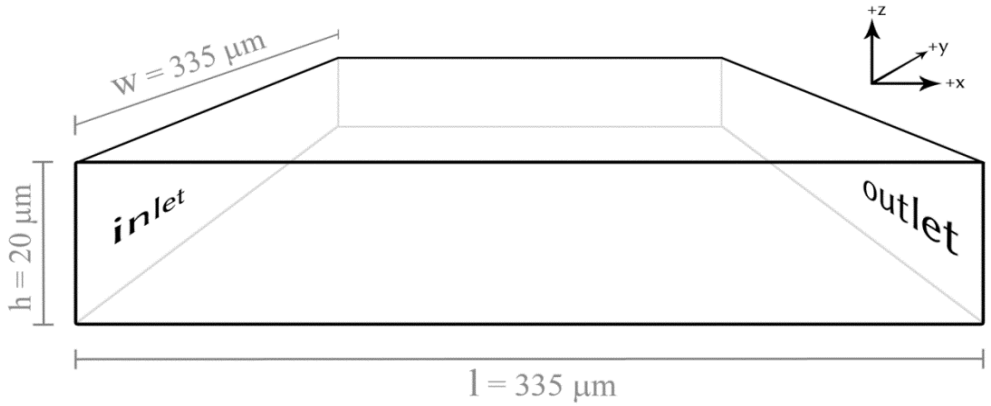

Figure 11: Exterior channel geometry for all simulations. Depth is exaggerated. Benchmarking takes place in the geometry as shown, with solid walls on all sides except the inlet and outlet. Later simulations vary interior geometry and boundary conditions.

Average local percent error (LBM results relative to analytical solution) in the streamwise component of velocity, denoted E_{analy}, is plotted below over a range of Δx. The 3D LBM begins at error near 11% for the largest Δx and ends near 1% with lattice refinement. The 2D LBM shows little change in average error, remaining under 1% for all values of Δx considered. There is an increase in error from about 0.25% to 0.80% between $\Delta x = 1.25\ \mu m$ and $\Delta x = 0.625\ \mu m$ for the 2D LBM. The reason for this increase is unknown.

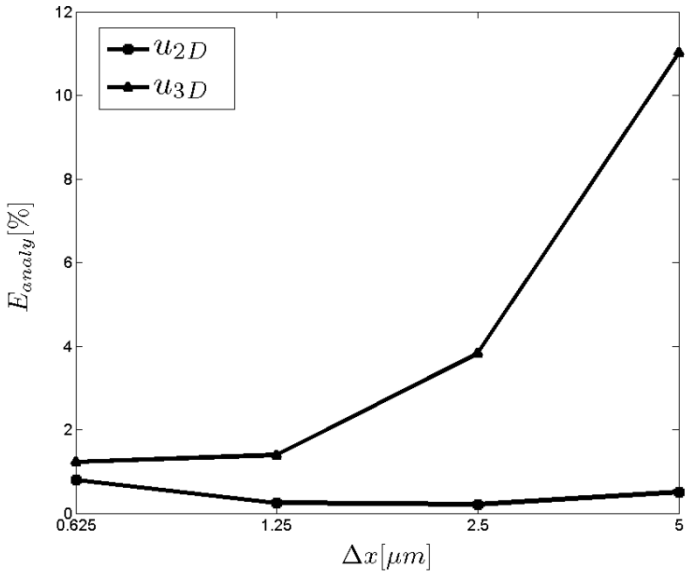

Figure 12: Average local error of 2D and 3D LBM velocity relative to analytical solutions for flow in an open rectangular channel. Average is taken over all fluid nodes. Lattice node spacing is varied between 5 and 0.625 micrometers.

4.2 Rapid Symmetric Contracting-Expanding Channel (RSCEC)

Flow is simulated in a rapidly contracting-expanding channel with a centered constriction formed by symmetric steps, with the purpose of testing $\boldsymbol{u_{2D}}(x, y)$ with rapid, symmetric depth variation. The height of each step is one quarter of the total channel depth, or 5 μm. The steps span the middle one-half of the channel length and the entire width. Flow is driven from left to right in Figure 13.

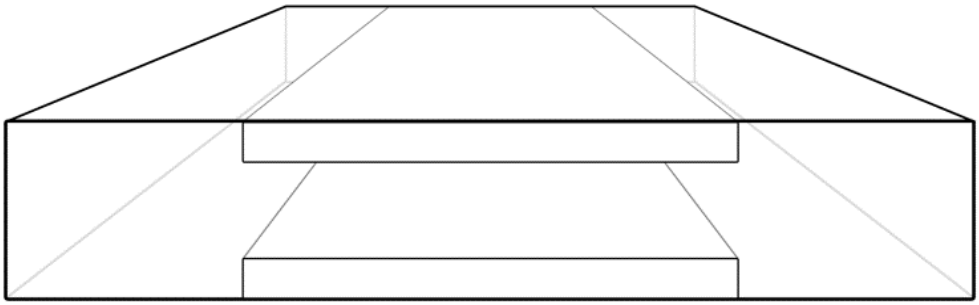

Figure 13: The rapid symmetric contracting-expanding channel (RSCEC) geometry. Centered steps reduce channel depth by half. Flow is driven from left to right.

The 3D velocity field $\boldsymbol{u_{3D}}(x, y, z)$ in this geometry has nonzero streamwise and vertical components, and zero transverse component. As previously noted, the vertical component of $\boldsymbol{u_{3D}}(x, y, z)$ is omitted from depth-averaging, leaving only the streamwise component nonzero in $\bar{\boldsymbol{u}}_{\boldsymbol{3D}}(x, y)$. Because the same is true of $\boldsymbol{u_{2D}}(x, y)$, it suffices to compare one-dimensional (1D) velocity profiles of the streamwise component averaged over the channel width. Note there is little variability over the width due to the periodic boundaries at $y = \pm w/2$. Still, $\bar{\boldsymbol{u}}_{\boldsymbol{3D}}(x, y)$ and $\boldsymbol{u_{2D}}(x, y)$ are width-averaged and compared in Figure 14. The 1D velocity profiles show qualitatively good agreement between the two methods with absolute error less than 1%, implying the assumption of a parabolic velocity profile in the vertical is fairly accurate, as verified by inspection in Figure 15. Table 1 contains maximum and average values of the streamwise component of velocity for both $\boldsymbol{u_{2D}}(x, y)$ and $\bar{\boldsymbol{u}}_{\boldsymbol{3D}}(x, y)$. In both cases, $\boldsymbol{u_{2D}}(x, y)$ underestimates $\bar{\boldsymbol{u}}_{\boldsymbol{3D}}(x, y)$ by less than one percent. The Reynolds number (Re) is also included in Table 1 to demonstrate the assumption of Stokes flow is satisfied. In this case, the characteristic length scale is twice the average channel depth $\bar{h}$.

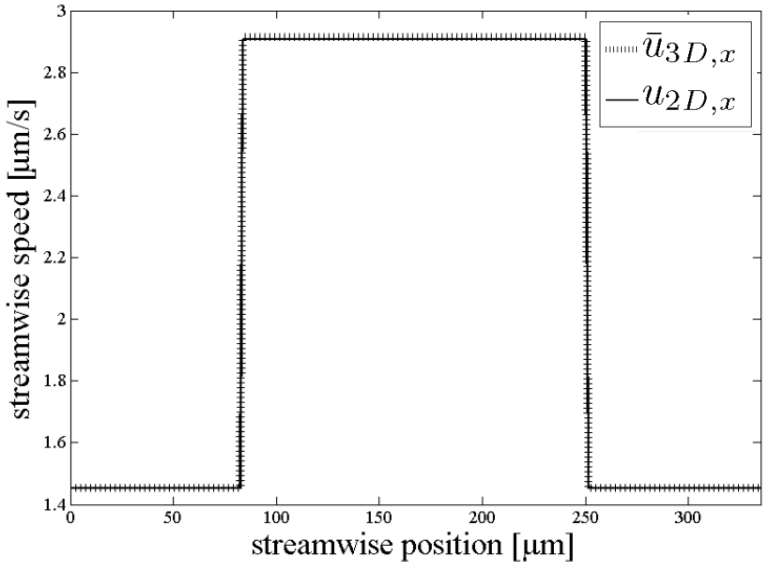

Figure 14: Width-averaged velocity profiles of the streamwise component of $\bar{u}_{3D}$ and u_{2D} in the rapid symmetric contracting-expanding channel.

Table 1: Streamwise component summary for the RSCEC. Maximum and average values of the streamwise (x) velocity component are reported, in addition to the Re in each simulation. Velocity in units of $\mu m/s$.

	$\max u_x^*$	$\langle u_x^* \rangle$	$Re = 2\langle u_x^* \rangle \bar{h}/\nu$
$\boldsymbol{u_{2D}}$	2.908	2.178	6.507×10^{-5}
$\boldsymbol{\bar{u}_{3D}}$	2.914	2.181	6.517×10^{-5}
$E_x[\%]$	-0.216	-0.142	

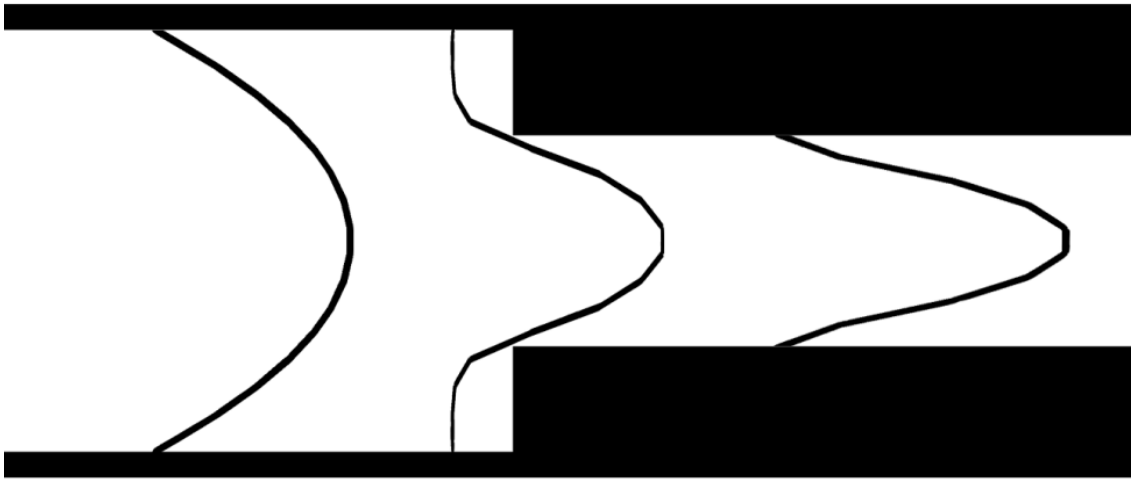

Figure 15: Profiles of the streamwise velocity component across the channel depth near the constriction in the RSCEC geometry. Profiles follow an approximately parabolic shape.

As previously discussed, the implicit depth with $\boldsymbol{u_{2D}}(x, y)$ may allow for more accurate determination of the velocity field in narrow constrictions across the channel depth, where $\overline{\boldsymbol{u}}_{\boldsymbol{3D}}(x, y)$ will produce inaccurate results with less than four fluid nodes. To demonstrate, we perform additional experiments in the RSCEC geometry. The results in Figure 14 and Table 1 were obtained by allowing the steps to block half the channel depth, leaving eight fluid nodes ($n = 8$) or a physical length of 10 μm within the constriction, whether it be explicitly or implicitly defined. We reduce the number of fluid nodes in the constriction to test the accuracy of both approaches, i.e. where $\overline{\boldsymbol{u}}_{\boldsymbol{3D}}(x, y)$ and $\boldsymbol{u_{2D}}(x, y)$ diverge or converge to an unrealistic result. Recall that in Figure 14, the streamwise component of velocity approximately doubles within the constriction, where the depth has been halved. In general, the ratio of the streamwise component in the constriction to that outside ($R_{\boldsymbol{u}^*}$) equals the ratio of the depth outside the constriction to that inside (R_h). As seen in Figure 14, velocity is constant within the constriction and outside it. The results are summarized in Table 2 and plotted in Figure 16.

Table 2: Ratio of depth (R_h) and streamwise velocity component (R_{u^*}) change due to flow constriction in RSCEC geometry. Velocity ratio is streamwise component inside constriction to that outside. Depth ratio is depth outside constriction to that inside. The number of fluid nodes within the constriction is n.

		R_h	R_{u^*}
$n = 8$ ($10\ \mu m$)	$\boldsymbol{u_{2D}}$	2	2.0008
	$\boldsymbol{\bar{u}_{3D}}$	2	2.005
$n = 6$ ($7.5\ \mu m$)	$\boldsymbol{u_{2D}}$	2.67	2.6706
	$\boldsymbol{\bar{u}_{3D}}$	2.67	2.6871
$n = 4$ ($5\ \mu m$)	$\boldsymbol{u_{2D}}$	4	4.0181
	$\boldsymbol{\bar{u}_{3D}}$	4	4.1301
$n = 2$ ($2.5\ \mu m$)	$\boldsymbol{u_{2D}}$	8	8.3411
	$\boldsymbol{\bar{u}_{3D}}$	8	12.3643
$n = 1$ ($1.25\ \mu m$)	$\boldsymbol{u_{2D}}$	16	23.1739
	$\boldsymbol{\bar{u}_{3D}}$	16	-0.2162

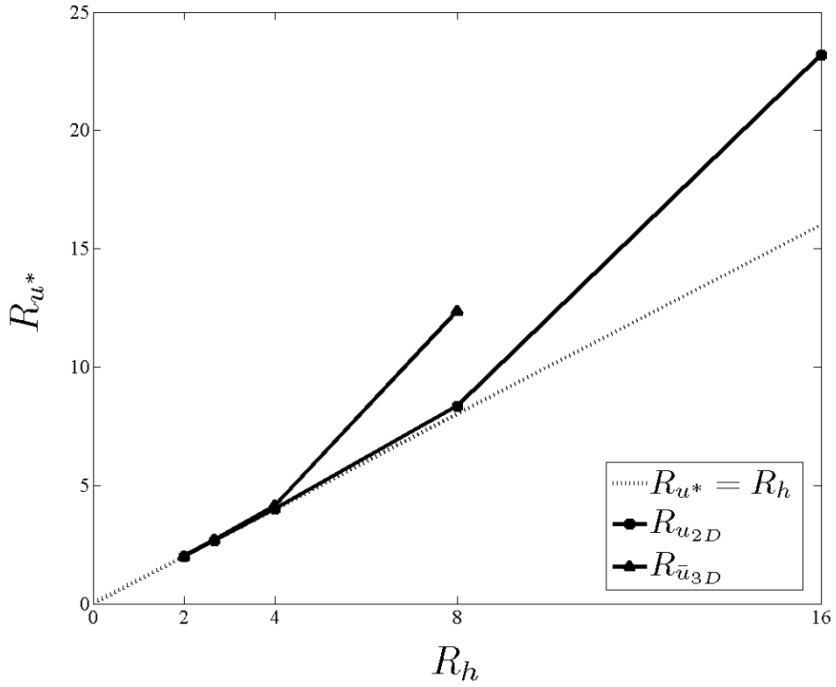

Figure 16: Velocity and depth ratios for the streamwise velocity component of $\bar{\boldsymbol{u}}_{\boldsymbol{3D}}$ and $\boldsymbol{u}_{\boldsymbol{2D}}$ in the RSCEC geometry with narrowing constriction.

$\bar{\boldsymbol{u}}_{\boldsymbol{3D}}(x, y)$ rapidly diverges from the identity line when there are fewer than 4 fluid nodes spanning the constriction ($R_h > 4$), as expected. $\boldsymbol{u}_{\boldsymbol{2D}}(x, y)$ also loses accuracy with a narrowing constriction, but to a lesser extent. Interestingly, $\bar{\boldsymbol{u}}_{\boldsymbol{3D}}(x, y)$ and therefore the 3D LBM, converges with only a single fluid node within the constriction, although the result differs substantially from that given by $\boldsymbol{u}_{\boldsymbol{2D}}(x, y)$. $R_{\bar{\boldsymbol{u}}_{\boldsymbol{3D}}}$ is negative because there is reverse flow (against the pressure gradient) outside the constriction, while forward flow within the constriction. In addition, $R_{\bar{\boldsymbol{u}}_{\boldsymbol{3D}}}$ is less than one because the velocity magnitude is larger outside the constriction. At this extremely shallow aspect ratio, $R_{\boldsymbol{u}_{\boldsymbol{2D}}}$ diverges significantly from R_h, but does not include any reverse flow.

4.3 Rapid Asymmetric Contracting-Expanding Channel (RACEC)

The RACEC geometry is equivalent to the RSCEC geometry in depth variation; one-half the depth is blocked within the centered constriction. This geometry differs in that the depth variation is imposed asymmetrically, with the purpose of testing $\boldsymbol{u_{2D}}(x, y)$ with rapid, asymmetric depth variation.

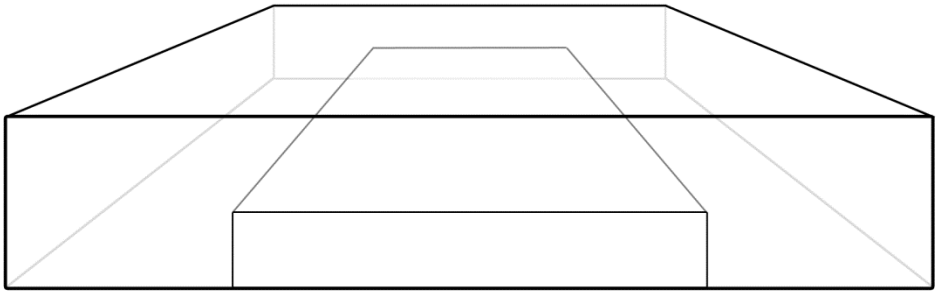

Figure 17: The rapid asymmetric contracting-expanding channel (RACEC).

Figure 18 plots the 1D width-averaged velocity profiles of the streamwise component of $\boldsymbol{u_{2D}}(x, y)$ and $\bar{\boldsymbol{u}}_{\boldsymbol{3D}}(x, y)$. The velocity profiles appear nearly identical to those in Figure 14, for the RSCEC. The maximum and average values of the streamwise component, however, show slightly larger error compared to the previous test geometry. The added error may be attributed to asymmetric depth variation, that being the only difference between the two geometries. Recall the assumption of a parabolic velocity profile across the channel depth implies the assumption of symmetry across the horizontal plane. The RACEC clearly violates this assumption, which may explain the greater error compared to the RSCEC. As in the previous test geometry, $\boldsymbol{u_{2D}}(x, y)$ underestimates $\bar{\boldsymbol{u}}_{\boldsymbol{3D}}(x, y)$ in both average and maximum value of the streamwise component.

Table 3: Streamwise component summary for the rapid asymmetric contracting-expanding channel (RACEC). Maximum and average values of the streamwise (x) velocity component are reported, in addition to the $\boldsymbol{Re}$ in each simulation. Velocity in units of $\boldsymbol{\mu m/s}$.

	$\max u_x^*$	$\langle u_x^* \rangle$	$Re = 2\langle u_x^* \rangle \bar{h}/\nu$
$\boldsymbol{u_{2D}}$	2.860	2.141	6.406×10^{-5}
$\bar{\boldsymbol{u}}_{\boldsymbol{3D}}$	2.865	2.144	6.416×10^{-5}
$E_x[\%]$	-0.220	-0.145	

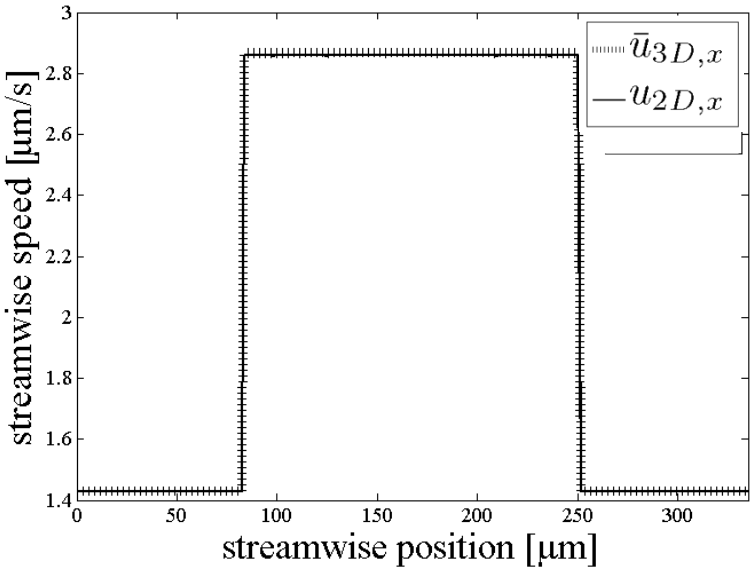

Figure 18: Width-averaged velocity profiles of the streamwise component of $\bar{u}_{3D}$ and u_{2D} in the rapid asymmetric contracting-expanding channel (RACEC).

4.4 Gradual Symmetric Contracting-Expanding Channel (GSCEC)

In the GSCEC geometry a series of steps, symmetric across the horizontal plane, span the entire width of the channel, with the purpose of testing $\boldsymbol{u_{2D}}(x, y)$ with repeated, symmetric variation in depth. All but the central step span one-eighth the streamwise length of the channel; the central step spans one-fourth the streamwise length. Step heights, from left to right in Figure 19, are 1.25, 5.0, 2.5, and 1.25 μm. The first and last eighth of the channel's streamwise length have no steps and therefore the maximum depth of 20 μm. The depth is reduced at most by half, as in the previous test geometries.

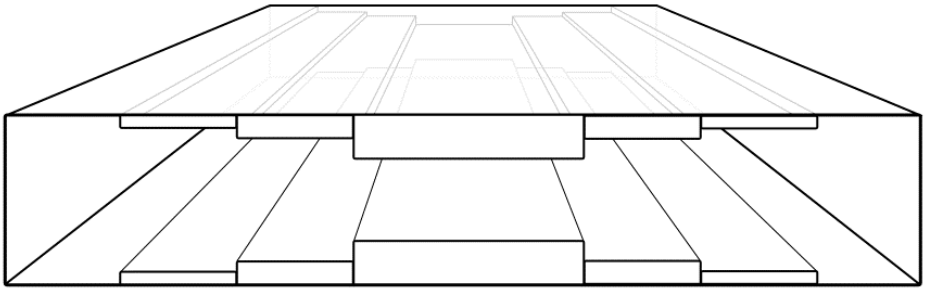

Figure 19: The gradual symmetric contracting-expanding channel (GSCEC).

Again, it suffices to compare 1D width-averaged velocity profiles. Figure 20 shows strong agreement between $\boldsymbol{u_{2D}}(x, y)$ and $\overline{\boldsymbol{u}}_{\boldsymbol{3D}}(x, y)$. Table 4 reports the maximum and average value of the streamwise component of velocity. In both cases, $\boldsymbol{u_{2D}}(x, y)$ underestimates $\overline{\boldsymbol{u}}_{\boldsymbol{3D}}(x, y)$ by less than one percent. The same measures of error were greater in both the RSCEC and RACEC geometries, possibly due to the more rapid depth variation. Recall the underlying assumption in obtaining $\boldsymbol{u_{2D}}(x, y)$ that the velocity profile across the implicit channel depth is parabolic. This assumption derived from considering flow in a constant-depth channel. As we stray from constant depth by varying the depth more severely, it is reasonable to expect the assumption of a parabolic profile to be violated, resulting in greater error.

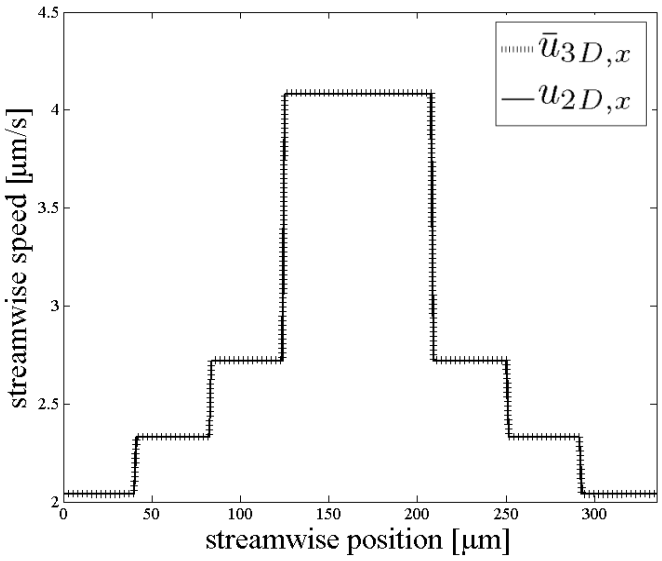

Figure 20: Width-averaged velocity profiles of the streamwise component of $\overline{\boldsymbol{u}}_{\boldsymbol{3D}}$ and $\boldsymbol{u_{2D}}$ in the gradual symmetric contracting-expanding channel (GSCEC).

Table 4: Streamwise component summary for the gradual symmetric contracting-expanding channel (GSCEC). Maximum and average values of the streamwise (x) velocity component are reported, in addition to the Re in each simulation. Velocity in units of $\mu m/s$.

	$\max u_x^*$	$\langle u_x^* \rangle$	$Re = 2\langle u_x^* \rangle \bar{h}/\nu$
$\boldsymbol{u_{2D}}$	4.080	2.789	8.691×10^{-5}
$\overline{\boldsymbol{u}}_{\boldsymbol{3D}}$	4.088	2.792	8.700×10^{-5}
$E_x[\%]$	-0.188	-0.107	

4.5 Gradual Asymmetric Contracting-Expanding Channel (GACEC)

In the GACEC a series of steps along the channel bottom, whose heights are double those of the previous test geometry, vary the channel depth with the purpose of testing $\boldsymbol{u_{2D}}(x, y)$ with repeated, asymmetric depth variation. The step heights from left to right in Figure 21 are 2.5, 5, 10, 5 and 2.5 μm, respectively. All other properties, such as the streamwise and transverse extent of each step, are equivalent to the GSCEC.

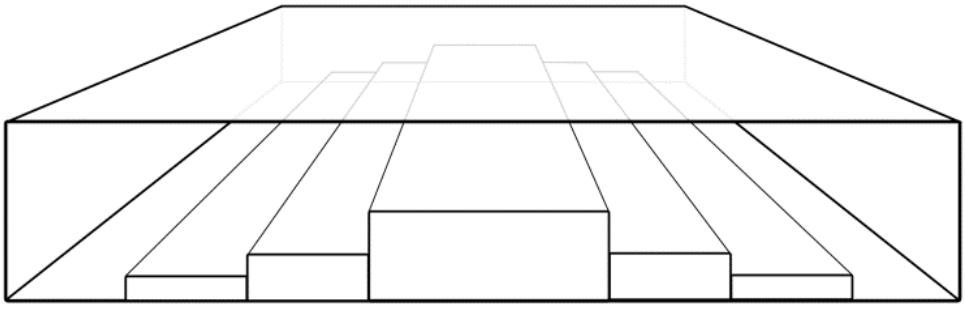

Figure 21: The gradual asymmetric contracting-expanding channel (GACEC).

1D width-averaged velocity profiles are plotted in Figure 22, showing strong agreement between $\boldsymbol{u_{2D}}(x, y)$ and $\overline{\boldsymbol{u}}_{\boldsymbol{3D}}(x, y)$. Table 5 summarizes properties of the streamwise component of

velocity, as in previous test cases. $\boldsymbol{u_{2D}}(x, y)$ underestimates $\overline{\boldsymbol{u}}_{\boldsymbol{3D}}(x, y)$ by less than one percent in both maximum and average values.

Table 5: Streamwise component summary for the gradual asymmetric contracting-expanding channel (GACEC). Maximum and average values of both streamwise (x) and transverse (y) velocity components are reported, in addition to the Re in each simulation. Velocity in units of $\mu m/s$.

	$\max u_x^*$	$\langle u_x^* \rangle$	$Re = 2\langle u_x^* \rangle \bar{h}/\nu$
$\boldsymbol{u_{2D}}$	4.005	2.738	8.530×10^{-5}
$\overline{\boldsymbol{u}}_{\boldsymbol{3D}}$	4.012	2.741	8.540×10^{-5}
$E_x[\%]$	-0.192	-0.113	

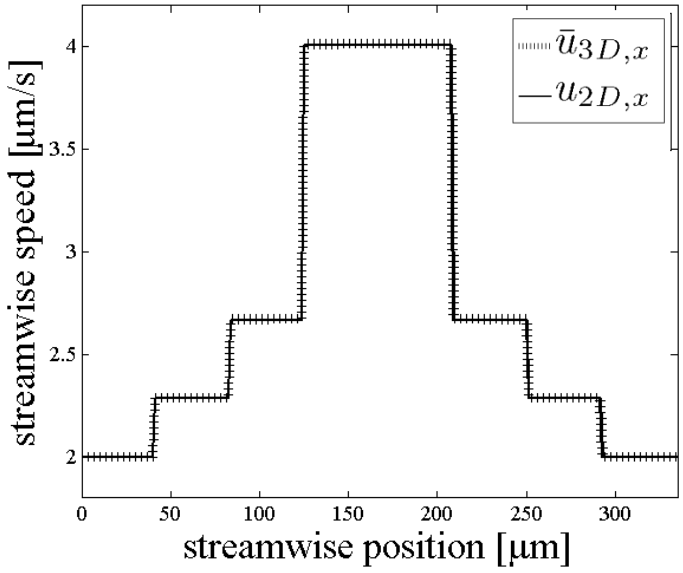

Figure 22: Width-averaged velocity profiles of the streamwise component of $\overline{\boldsymbol{u}}_{\boldsymbol{3D}}$ and $\boldsymbol{u_{2D}}$ in the gradual asymmetric contracting-expanding channel (GACEC).

We now summarize the results of the four contracting-expanding channel geometries. The error in $\langle u_x^* \rangle$ for each is reported in Table 6. All are negative, suggesting $\boldsymbol{u_{2D}}(x, y)$ has a bias toward underestimating $\overline{\boldsymbol{u}}_{\boldsymbol{3D}}(x, y)$ in this general type of geometry. Rapid and asymmetric depth

variation result in greater absolute error compared to gradual and symmetric depth variation, respectively. This result is likely due to decreasing accuracy of the underlying assumption used in obtaining $\boldsymbol{u_{2D}}(x, y)$, namely a parabolic velocity profile across the channel vertical. Also, a change from gradual to rapid depth variation results in greater added error than a change from symmetric to asymmetric variation. This result suggests the underlying assumption is violated more severely with the rate of depth variation than its symmetry.

Table 6: Summary of contracting-expanding channels: reported values are percent error in $\langle u_x^* \rangle$.

	symmetric	asymmetric
rapid	-0.142	-0.145
Gradual	-0.107	-0.113

4.6 Constant-Depth Channel with Complete Cylindrical Pillar (CCP)

A single cylindrical pillar is centered in a constant-depth channel. The pillar's diameter spans one-half the channel's streamwise length and width, and its height spans the entire channel depth. Unlike the previous four geometries, this will test $\boldsymbol{u_{2D}}(x, y)$ with both components of velocity being nonzero in the horizontal plane.

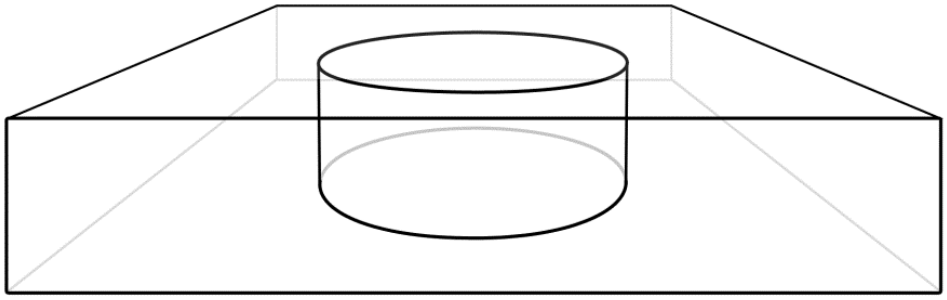

Figure 23: The constant-depth channel with complete cylindrical pillar (CCP).

Streamlines are plotted in Figure 24 to qualitatively compare $\boldsymbol{u_{2D}}(x, y)$ and $\overline{\boldsymbol{u}}_{\boldsymbol{3D}}(x, y)$. The two sets of streamlines begin to separate near the streamwise front end of the cylinder, and rejoin

near the streamwise back end. This characteristic is explained by the left and right periodic boundaries as well as the geometry's symmetry. Streamlines near the cylinder appear to separate more than those further away. This property is explained by considering the differences in each component of velocity, reported in

Table 7. Note the numbers reported in

Table 7 for the transverse component take its absolute value because there is both positive and negative transverse flow in this geometry, unlike any of the previous. The transverse component shows larger absolute error in both maximum and average values over all fluid nodes. Transverse flow is greatest near the cylinder, particularly near its streamwise front and back, coinciding with the largest separation in streamlines.

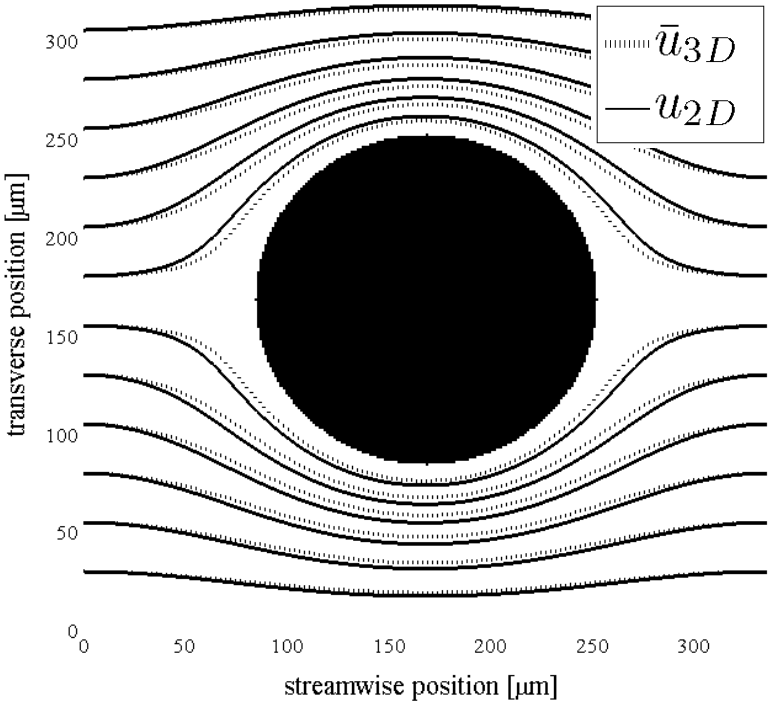

Figure 24: Streamlines of flow around a complete cylinder pillar.

Table 7: Velocity field summary for the complete cylindrical pillar (CCP). Maximum and average values of both streamwise (x) and transverse (y) velocity components are reported, in addition to the $\boldsymbol{Re}$ in each simulation. Velocity in units of $\boldsymbol{\mu m/s}$.

	$\max u_x^*$	$\langle u_x^* \rangle$	$\max\lvert u_y^* \rvert$	$\langle \lvert u_y^* \rvert \rangle$	$Re = \langle \lVert \boldsymbol{u}^* \rVert \rangle d/\nu$
$\boldsymbol{u_{2D}}$	10.212	4.2705	2.841	0.810	7.382×10^{-4}
$\boldsymbol{\bar{u}_{3D}}$	9.716	4.2702	3.790	0.817	7.401×10^{-4}
$E_i[\%]$	5.11	0.00703	-25.0	-0.850	

In general, $\boldsymbol{u_{2D}}(x, y)$ overestimates the streamwise component and underestimates the transverse component. The average values for both velocity components show good agreement between $\boldsymbol{u_{2D}}(x, y)$ and $\boldsymbol{\bar{u}_{3D}}(x, y)$, with less than one percent difference, while the maximum values show the largest absolute errors so far. The average of the transverse component is underestimated by about two orders of magnitude greater than the streamwise component is overestimated. Similarly, the transverse component's maximum is underestimated more severely than the streamwise component's maximum is overestimated.

Table 7 also reports the Reynolds number for each flow, defined with the average velocity magnitude $\langle \lVert \boldsymbol{u}^* \rVert \rangle$ and cylinder diameter d.

4.7 Constant-depth Channel with Partial Cylindrical Pillar (PCP)

Flow is simulated in a geometry similar to the CCP, except the cylindrical pillar does not span the entire channel depth. Instead, the middle one-half of the pillar's height is removed. The partial pillar is centered in the channel and has a diameter spanning one-half the channel's length and width. This geometry will test $\boldsymbol{u_{2D}}(x, y)$ with two nonzero components of velocity in the horizontal plane with depth variation, unlike the previous test geometries. Note that unlike in the CCP test case, the 2D geometry here does not include a cylindrical pillar. This geometry is similar to the contracting-expanding channels examined earlier, except the step constriction does

not span the entire channel width.

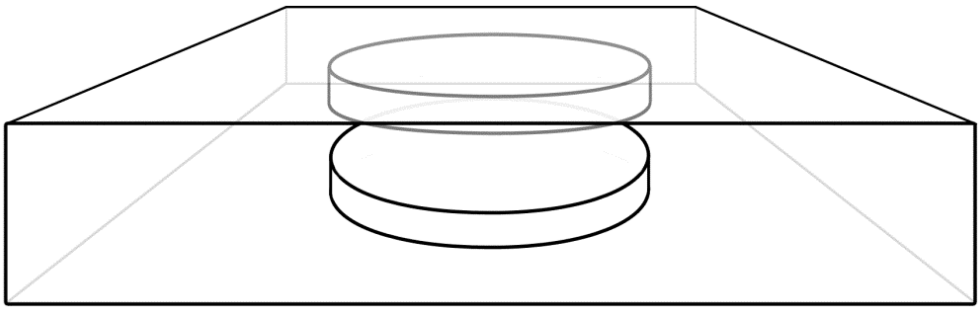

Figure 25: The constant-depth channel with partial cylindrical pillar (PCP).

$\boldsymbol{u_{2D}}(x, y)$ and $\overline{\boldsymbol{u}}_{\boldsymbol{3D}}(x, y)$ are compared via streamlines in Figure 26. The streamlines in this geometry are similar to those in the previous, with the exception of streamlines passing through the pillar's opening. Because some flow passes through the opening, streamlines away from the partial pillar are more flat, i.e. with smaller transverse component, relative to the streamlines for the CCP. Streamlines first separate near the streamwise front of the partial pillar and reconnect near the back. The discrepancy between streamlines is most significant inside the partial pillar's opening. Because depth is varied rapidly near the partial pillar, akin to the RSCEC and RACEC, error is expected to be most significant nearby.

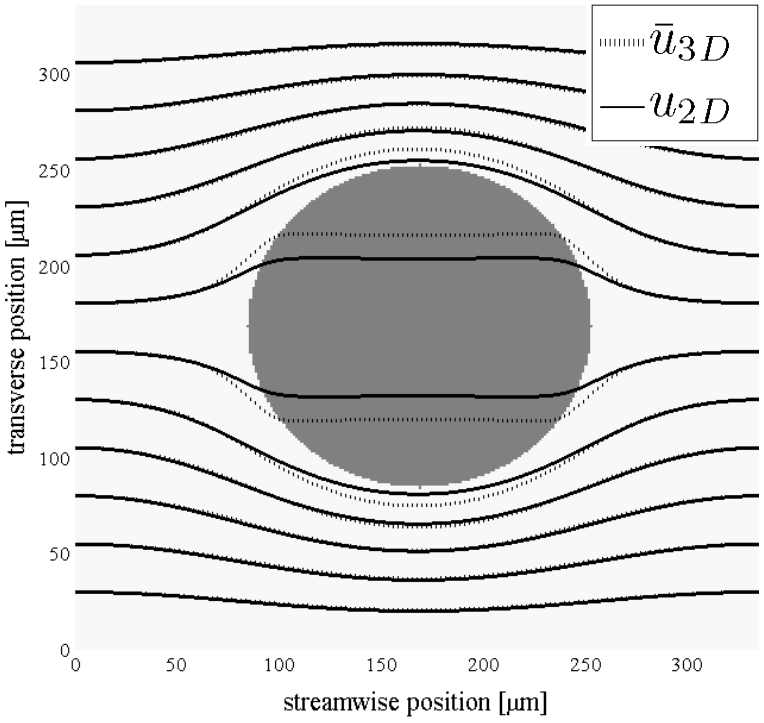

Figure 26: Streamlines of flow around and through a partial cylindrical pillar.

Table 8: Velocity field summary for the partial cylindrical pillar (PCP). Maximum and average values of both streamwise (x) and transverse (y) velocity components are reported, in addition to the Re in each simulation. Velocity in units of $\mu m/s$.

	$\max u_x^*$	$\langle u_x^* \rangle$	$\max\lvert u_y^* \rvert$	$\langle \lvert u_y^* \rvert \rangle$	$Re = \langle \lVert \boldsymbol{u}^* \rVert \rangle d/\nu$
$\boldsymbol{u_{2D}}$	8.723	4.966	2.179	0.657	8.426×10^{-4}
$\bar{\boldsymbol{u}}_{\boldsymbol{3D}}$	9.306	4.874	3.286	0.714	8.322×10^{-4}
$E_i[\%]$	-6.26	1.88	-33.7	-7.94	

Both components of the velocity field are reported in Table 8. The closest agreement between $\boldsymbol{u_{2D}}(x, y)$ and $\bar{\boldsymbol{u}}_{\boldsymbol{3D}}(x, y)$ is in the average streamwise component, in line with previous results. The average streamwise component is overestimated by $\boldsymbol{u_{2D}}(x, y)$; all other metrics considered in the table are underestimated. The absolute errors in maximum and average transverse component are larger than those for the streamwise component, also in line with

previous results. The absolute errors reported in Table 8 are the largest yet, which is reasonable considering the flow is the most complex yet.

4.8 Constant-Depth Unit Cell (UC)

The unit cell is a representative section of the MFD, depicted in Figure 27. It contains a central cylindrical pillar and a quarter pillar centered on each vertical edge of the domain. All pillars span the entire channel depth. The unit cell geometry will test $\boldsymbol{u_{2D}}(x, y)$ with a more complex flow in the horizontal plane, relative to the CCP geometry, with no vertical component of velocity because the channel depth is constant.

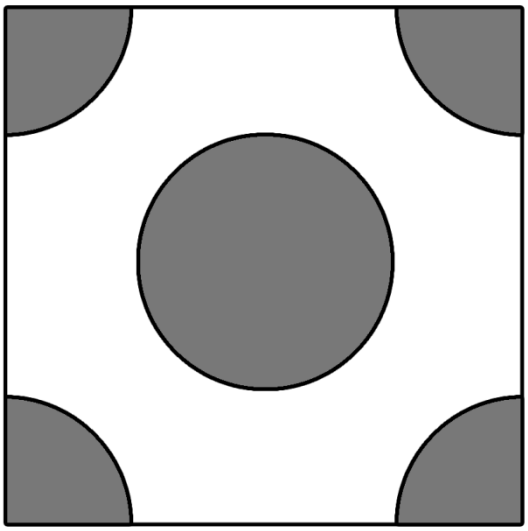

Figure 27: The constant-depth unit cell geometry (planar view).

Streamlines for $\boldsymbol{u_{2D}}(x, y)$ and $\overline{\boldsymbol{u}}_{\boldsymbol{3D}}(x, y)$ are plotted in Figure 28. In the two previous test cases, streamlines matched well away from the central pillar. This is not the case in the unit cell geometry. Streamlines show their maximum separation away from the central pillar. As noted earlier, streamlines appear to separate in regions of significant transverse flow. Pillars on each corner of the plane result in significant transverse flow throughout nearly the entire domain, except near the top and bottom edges, where the streamlines agree relatively well. Symmetry in the horizontal plane results in streamlines that begin and end in agreement. Suppose the

geometry was not symmetric in the horizontal plane. Then the discrepancy in streamlines produced in the left half plane may not "reverse" itself in the right half plane. Therefore, it is possible in simulating flow in an irregular geometry that early error, characterized by streamline discrepancy, could propagate and increase downstream. We note this possibility as a consideration for applying and extending the current work.

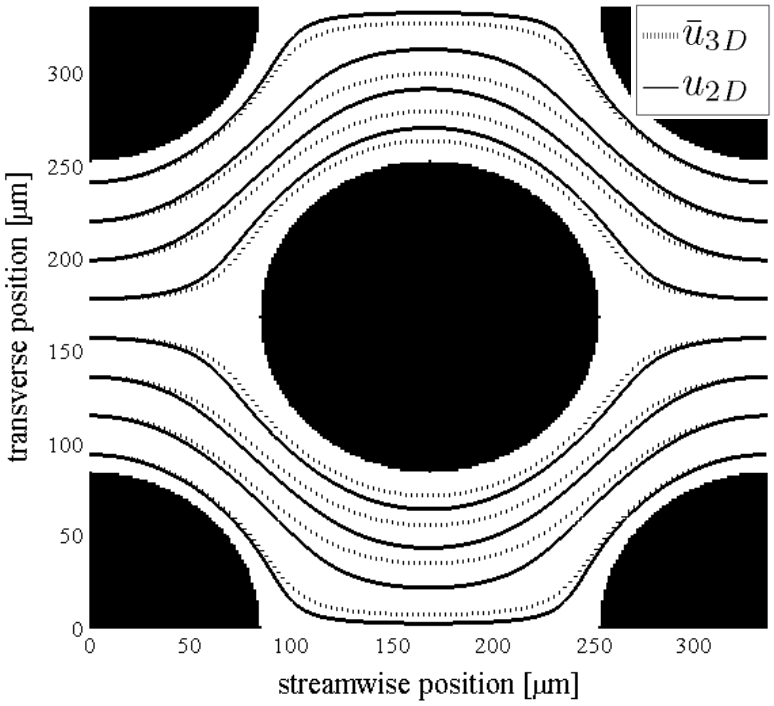

Figure 28: Streamline comparison for flow in the unit cell.

Properties of the velocity components are summarized in Table 9. The best agreement between $\boldsymbol{u_{2D}}(x, y)$ and $\boldsymbol{\bar{u}_{3D}}(x, y)$ is in the average streamwise component of velocity, where the error is less than one percent. The maximum of the streamwise component is underestimated by $\boldsymbol{u_{2D}}(x, y)$, while all other metrics considered in the table are overestimated. As before, the streamwise component of $\boldsymbol{\bar{u}_{3D}}(x, y)$ is better approximated by $\boldsymbol{u_{2D}}(x, y)$ than the transverse component.

Table 9: Velocity field summary for the unit cell (UC) with cylindrical pillars. Maximum and average values of both streamwise (x) and transverse (y) velocity components are reported, in addition to the $\boldsymbol{Re}$ in each simulation. Velocity in units of $\boldsymbol{\mu m/s}$.

	$\max u_x^*$	$\langle u_x^* \rangle$	$\max\lvert u_y^* \rvert$	$\langle \lvert u_y^* \rvert \rangle$	$Re = \langle \lVert \boldsymbol{u}^* \rVert \rangle d/\nu$
$\boldsymbol{u_{2D}}$	6.028	2.4893	5.905	1.362	4.953×10^{-4}
$\boldsymbol{\bar{u}_{3D}}$	6.184	2.4886	4.751	1.219	4.831×10^{-4}
$E_i[\%]$	-2.52	0.0281	24.3	11.7	

4.9 Random-depth Channel (RDC)

Channel depth is varied randomly following a log-normal distribution with spatial correlation and Gaussian power spectrum type (Interactive Models for Groundwater Flow and Solute Transport), to provide smoothness in the local channel depth $h(x, y)$. The distribution has a mean of 15 μm and variance of 5 μm. Correlation length in both the streamwise and transverse directions is 40 μm, approximately one-tenth the length or width of the channel. The depth is allowed to take integer values between 10 μm and 20 μm, inclusive. Any values generated outside this range are rounded to the nearest endpoint, i.e. 10 μm or 20 μm. Depth is varied nearly symmetrically across the horizontal plane in the 3D lattice. If the local depth requires an even number of solid nodes, they are allocated equally above and below the horizontal plane. If an odd number of solid nodes are required, one extra solid node is assigned above the horizontal plane. The purpose of this geometry is to test $\boldsymbol{u_{2D}}(x, y)$ with irregular 2D depth variation. Streamlines of $\boldsymbol{u_{2D}}(x, y)$ and $\boldsymbol{\bar{u}_{3D}}(x, y)$ are plotted in Figure 29, along with a map of $h(x, y)$. Although there is significant depth variation in both the streamwise and transverse directions, the streamlines are mostly horizontal. They converge in regions of relatively large channel depth ($\approx 20\ \mu m$) and diverge in regions of relatively small channel depth ($\approx 10\ \mu m$). The streamlines of $\boldsymbol{u_{2D}}(x, y)$ and $\boldsymbol{\bar{u}_{3D}}(x, y)$ show good agreement despite the geometry's irregularity.

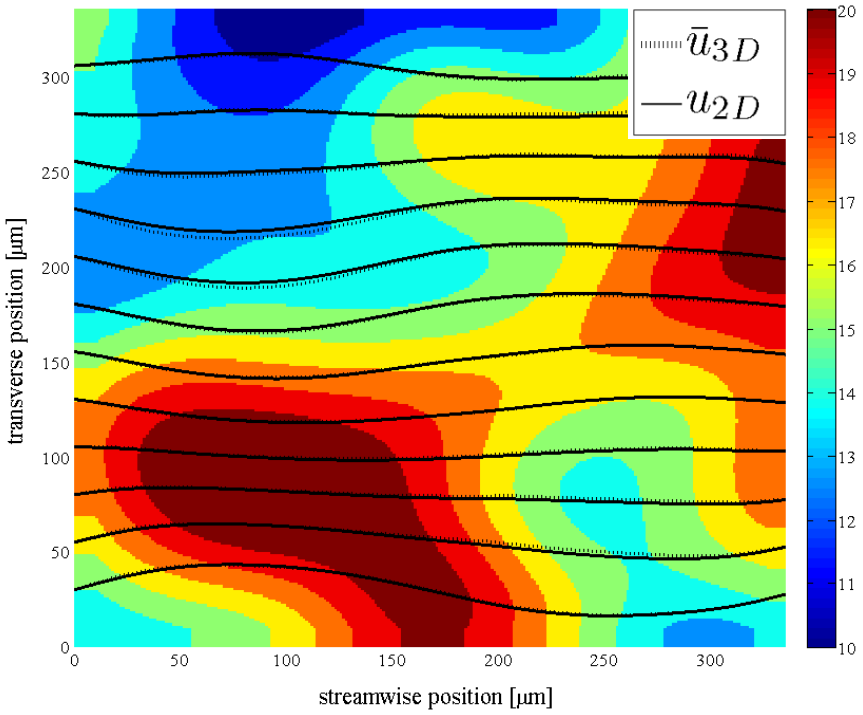

Figure 29: Streamlines in the random-depth channel and $\boldsymbol{h(x,y)}$.

Table 10: Velocity field summary for the random-depth channel (RDC). Maximum and average values of both streamwise (x) and transverse (y) velocity components are reported, in addition to the $\boldsymbol{Re}$ in each simulation. Velocity in units of $\boldsymbol{\mu m/s}$.

	$\max u_x^*$	$\langle u_x^* \rangle$	$\max \lvert u_y^* \rvert$	$\langle \lvert u_y^* \rvert \rangle$	$Re = \langle \lVert \boldsymbol{u}^* \rVert \rangle d/\nu$
$\boldsymbol{u_{2D}}$	7.661	4.826	1.803	0.468	1.538×10^{-4}
$\boldsymbol{\bar{u}_{3D}}$	7.478	4.800	2.243	0.488	1.531×10^{-4}
$E_i[\%]$	2.45	0.535	−19.62	−4.10	

As reported in Table 10, the streamwise component of velocity is overestimated by $\boldsymbol{u_{2D}}(x,y)$ in both average and maximum value, while the transverse component is underestimated. As in previous geometries, average values for each component show better agreement than maximum values. In the four contracting-expanding channel geometries, $\boldsymbol{u_{2D}}(x,y)$ consistently underestimated the streamwise component of velocity in both maximum and average value. In

those cases, the transverse component of velocity was zero. The current geometry has nonzero, although relatively little, transverse flow, seen by comparing the magnitudes of $\max u_i^*$ and $\langle u_i^* \rangle$. In the random-depth channel, $\boldsymbol{u_{2D}}(x, y)$ overestimates the streamwise component in both maximum and average value, suggesting the negative bias in streamwise component observed in earlier geometries is dependent on the transverse component.

4.10 Unit Cell with Random Depth (UCRD)

The final geometry is a unit cell with random depth, representative of the expected geometry in a section of the MFD with significant precipitate accumulation on the top and bottom surfaces. The depth field $h(x, y)$ used previously in the random-depth channel defines local depth around the cylindrical pillars. Thus, the current geometry is simply a composition of the UC and RDC geometries. As before, the channel depth may be constricted by at most one-half its maximum value.

Streamlines of $\boldsymbol{u_{2D}}(x, y)$ and $\overline{\boldsymbol{u}}_{\boldsymbol{3D}}(x, y)$ are plotted in Figure 30, along with a map of $h(x, y)$. The irregular depth results in greater separation of streamlines relative to the unit cell geometry with constant depth. In addition, streamlines do not converge past the streamwise back of the central cylinder, as they did in the previous unit cell geometry due to its symmetry. If the domain were extended further downstream, the discrepancy in streamlines would propagate, and likely grow with length if the depth continued to be irregular. In general, $\boldsymbol{u_{2D}}(x, y)$ may approximate $\overline{\boldsymbol{u}}_{\boldsymbol{3D}}(x, y)$ more poorly with streamwise length in a realistic, i.e. arbitrary depth, MFD geometry.

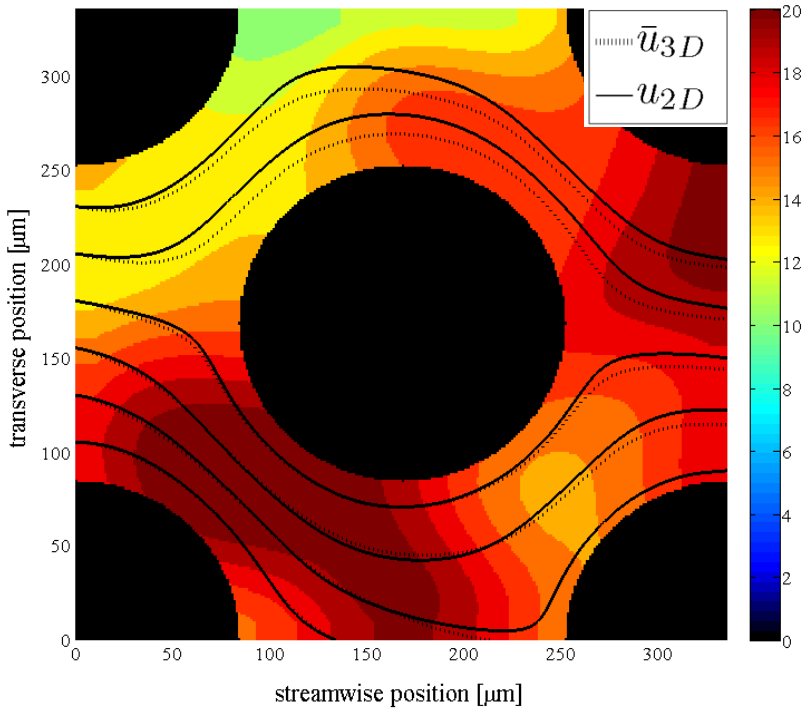

Figure 30: Streamlines in the unit cell with random depth and $h(x, y)$.

Table 11: Velocity field summary for the unit cell with random depth (UCRD). Maximum and average values of both streamwise (x) and transverse (y) velocity components are reported, in addition to the Re in each simulation. Velocity in units of $\mu m/s$.

	$\max u_x^*$	$\langle u_x^* \rangle$	$\max \lvert u_y^* \rvert$	$\langle \lvert u_y^* \rvert \rangle$	$Re = \langle \lVert \boldsymbol{u}^* \rVert \rangle d/\nu$
$\boldsymbol{u_{2D}}$	6.353	1.807	5.125	1.012	3.014×10^{-4}
$\boldsymbol{\bar{u}_{3D}}$	6.334	1.778	4.443	0.946	2.967×10^{-4}
$E_i[\%]$	0.292	1.58	15.3	6.97	

$\boldsymbol{u_{2D}}(x, y)$ overestimates $\overline{\boldsymbol{u}}_{\boldsymbol{3D}}(x, y)$ in maximum and average value for both velocity components. Absolute error is larger for the transverse component, as in all other test geometries with nonzero transverse flow. Because the current geometry is a composition of two previous geometries, we compare the errors for each in Table 12. One may expect a worse performance by $\boldsymbol{u_{2D}}(x, y)$ in the UCRD geometry, compared to the UC or RDC geometries, because it is more complex. In the average streamwise component, this is the case. In all other metrics considered, $\boldsymbol{u_{2D}}(x, y)$ performs worst in the UC geometry. Although there appear to be some trends relating error to geometric features (see the summary of contracting-expanding channel geometries), the results summarized in Table 12 show that accuracy of $\boldsymbol{u_{2D}}(x, y)$ in approximating $\overline{\boldsymbol{u}}_{\boldsymbol{3D}}(x, y)$ is not always a simple function of the geometry complexity.

Table 12: Error summary for unit cell (UC), random-depth channel (RDC), and unit cell with random depth (UCRD) geometries. Reported values are percent error.

	$\max u_x^*$	$\langle u_x^* \rangle$	$\max \lvert u_y^* \rvert$	$\langle \lvert u_y^* \rvert \rangle$
UC	-2.52	0.0281	24.3	11.7
RDC	2.45	0.535	-19.62	-4.10
UCRD	0.292	1.58	15.3	6.97

4.11 Series of Unit Cells with Random Depth (SUCRD)

The final test geometry is a series of four unit cells with the purpose of studying downstream propagation of error between $\boldsymbol{u_{2D}}(x, y)$ and $\overline{\boldsymbol{u}}_{\boldsymbol{3D}}(x, y)$. The random spatially-correlated depth within each cell is identical to that used previously in the RDC and UCRD test geometries. Although concatenating unit cells results in abrupt depth change at each boundary, we expect $\boldsymbol{u_{2D}}(x, y)$ can handle this case considering the previously reported results of the contracting-expanding channels with rapid depth variation in Sections 4.2 and 4.3. Figure 31 plots streamlines for $\boldsymbol{u_{2D}}(x, y)$ and $\overline{\boldsymbol{u}}_{\boldsymbol{3D}}(x, y)$ against a map of the local channel depth.

Streamlines in the first cell behave as those in the UCRD geometry. Larger discrepancies develop beyond the first cell, seen by following any pair of streamlines, one each from $\boldsymbol{u_{2D}}(x, y)$ and $\overline{\boldsymbol{u}}_{\boldsymbol{3D}}(x, y)$ that begin at the same point on the west boundary. In some cases, the pair of streamlines splits around a pillar. In other cases, one streamline exits the south boundary while the other does not.

These differences in streamlines deal primarily with their behavior in the transverse direction. As observed in previous test geometries, and shown in Table 13 for this geometry, the transverse component of velocity is more poorly approximated than the streamwise component. Errors in the maximum and average value of the transverse velocity component are less than 15%. At this level of error, streamlines show the diverging behavior just described.

Table 13: Velocity field summary for the series of unit cells with random depth (SUCRD). Maximum and average values of both streamwise (x) and transverse (y) velocity components are reported, in addition to the $\boldsymbol{Re}$ in each simulation. Velocity in units of $\boldsymbol{\mu m/s}$.

	$\max u_x^*$	$\langle u_x^* \rangle$	$\max \lvert u_y^* \rvert$	$\langle \lvert u_y^* \rvert \rangle$	$Re = \langle \lVert \boldsymbol{u}^* \rVert \rangle d/\nu$
$\boldsymbol{u_{2D}}$	5.69	1.686	4.67	0.941	3.36×10^{-4}
$\overline{\boldsymbol{u}}_{\boldsymbol{3D}}$	5.75	1.657	4.12	0.889	3.27×10^{-4}
$E_i[\%]$	-1.08	1.732	13.2	5.84	

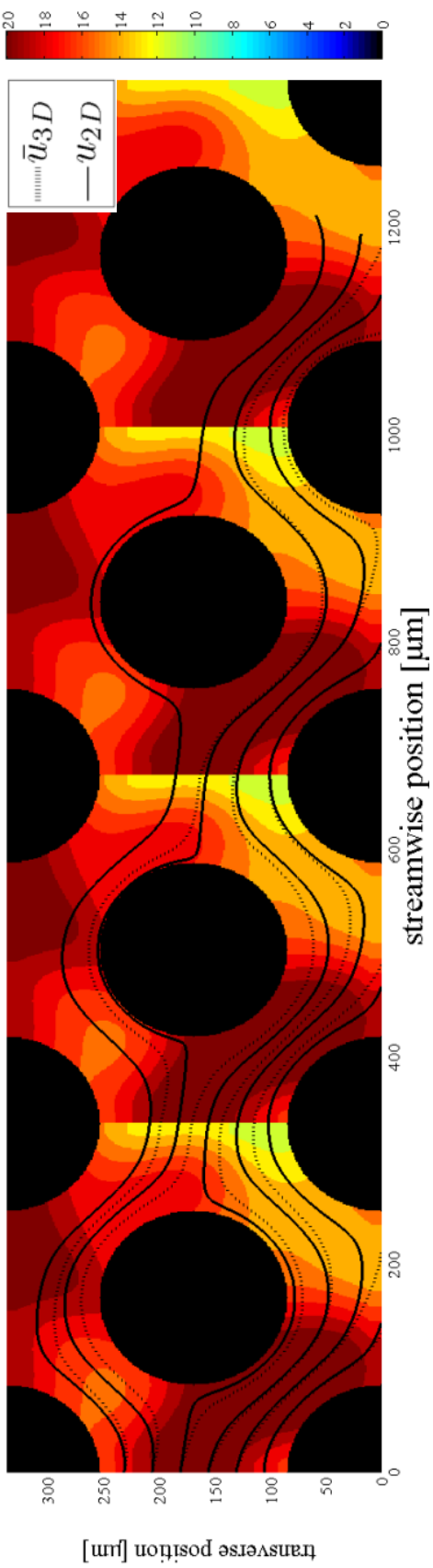

Figure 31: Streamlines in a series of four unit cells and the depth field, shown in color in units of μm. Streamlines for $\bar{u}_{3D}(x, y)$ are dashed lines, while those for $u_{2D}(x, y)$ are solid lines.

4.12 Comparison of Run Times

Table 14 reports the run time needed to solve for $\boldsymbol{u_{2D}}(x, y)$, denoted $RT_{\boldsymbol{u_{2D}}}$, the run time needed to solve for $\overline{\boldsymbol{u}}_{\boldsymbol{3D}}(x, y)$, denoted $RT_{\overline{\boldsymbol{u}}_{\boldsymbol{3D}}}$, and the ratio of the two, denoted S, for all ten geometries. All code is sequential and run on an Intel Core i5-3570 CPU. Repeated runs of the same simulation yielded run times within one second of each other. This variation has little effect on the value of S, so only the times for a single run are reported. S ranges from 3.7 to 10.1, with an average value of 6.9. As a rough approximation, solving the 2D governing equations is about seven times faster, on average, than solving 3D governing equations, at least across the ten geometries considered. While the 2D simulations have shorter run times, they require more iterations to converge. For example, in the GSCEC geometry $\boldsymbol{u_{2D}}(x, y)$ requires about 13,000 iterations to converge, while $\boldsymbol{u_{3D}}(x, y)$ requires about 3,000. In the UCRD geometry $\boldsymbol{u_{2D}}(x, y)$ requires about 17,000 iterations to converge, while $\boldsymbol{u_{3D}}(x, y)$ requires about 3,500.

Table 14: Simulation run time for $\boldsymbol{u_{2D}}$ ($\boldsymbol{RT_{u_{2D}}}$) and $\overline{\boldsymbol{u}}_{\boldsymbol{3D}}$ ($\boldsymbol{RT_{\overline{u}_{3D}}}$) in each test geometry in units of seconds. Ratio of run times $\boldsymbol{S = RT_{\overline{u}_{3D}}/RT_{u_{2D}}}$.

Geometry	$RT_{\boldsymbol{u_{2D}}}$	$RT_{\overline{\boldsymbol{u}}_{\boldsymbol{3D}}}$	$S = RT_{\overline{\boldsymbol{u}}_{\boldsymbol{3D}}}/RT_{\boldsymbol{u_{2D}}}$
RSCEC	49.4	493.9	10.0
RACEC	49.5	498.8	10.1
GSCEC	66.2	403.6	6.1
GACEC	49.4	497.2	10.1
CCP	132.5	656.6	5.0
PCP	155.7	573.5	3.7
UC	82.7	557.5	6.7
RDC	101.8	456.4	4.5
UCRD	62.5	419.4	6.7
SUCRD	294.8	1742.0	5.9

4.13 Effects of Velocity Field Scaling and the Viscous Drag Term

Two modifications are made to the standard 2D LBM so that $\boldsymbol{u_{2D}}(x, y)$ may more closely approximate $\overline{\boldsymbol{u}}_{\boldsymbol{3D}}(x, y)$. First, $\boldsymbol{u_{2D}}(x, y)$ is solved for with an external acceleration representing viscous drag from the top and bottom MFD surfaces. Second, after $\boldsymbol{u_{2D}}(x, y)$ is solved for it is uniformly scaled so its inlet flow rate equals that of $\overline{\boldsymbol{u}}_{\boldsymbol{3D}}(x, y)$**.** The effect of these modifications is studied by revisiting the unit cell with random depth geometry, shown earlier in Figure 30. Errors between $\boldsymbol{u_{2D}}(x, y)$ and $\overline{\boldsymbol{u}}_{\boldsymbol{3D}}(x, y)$ without scaling, without viscous drag, and with neither scaling nor viscous drag are reported in Table 15. Errors with scaling and viscous drag are reported again in the first row for comparison. The least absolute error for each category is marked by an asterisk.

Table 15: Error summary for the unit cell with random depth (UCRD) with and without scaling and viscous drag. Reported values are percent error of maximum and average values for both streamwise (x) and transverse (y) velocity components. The least absolute error for each category is marked by an asterisk.

	$\max u_x^*$	$\langle u_x^* \rangle$	$\max \lvert u_y^* \rvert$	$\langle \lvert u_y^* \rvert \rangle$
$E_i[\%]$	0.292	1.58	15.3*	6.97*
$E_i[\%]$ (no scaling)	-40.84	-40.07	-31.95	-36.903
$E_i[\%]$ (no viscous drag)	0.0647*	0.0321*	31.00	18.515
$E_i[\%]$ (no scaling or viscous drag)	167	149	208	169

For the maximum and average value of the streamwise component, the least absolute error comes from omitting the viscous drag term and scaling $\boldsymbol{u_{2D}}(x, y)$. This result suggests scaling can account for most of the effect of viscous drag for the streamwise velocity component, but not for the transverse. The poor agreement in transverse component is seen in Figure 32,

where streamlines are plotted for $\bar{\boldsymbol{u}}_{\boldsymbol{3D}}(x, y)$ and $\boldsymbol{u}_{\boldsymbol{2D}}(x, y)$ without viscous drag. The streamlines of $\boldsymbol{u}_{\boldsymbol{2D}}(x, y)$ behave as though the channel depth were constant.

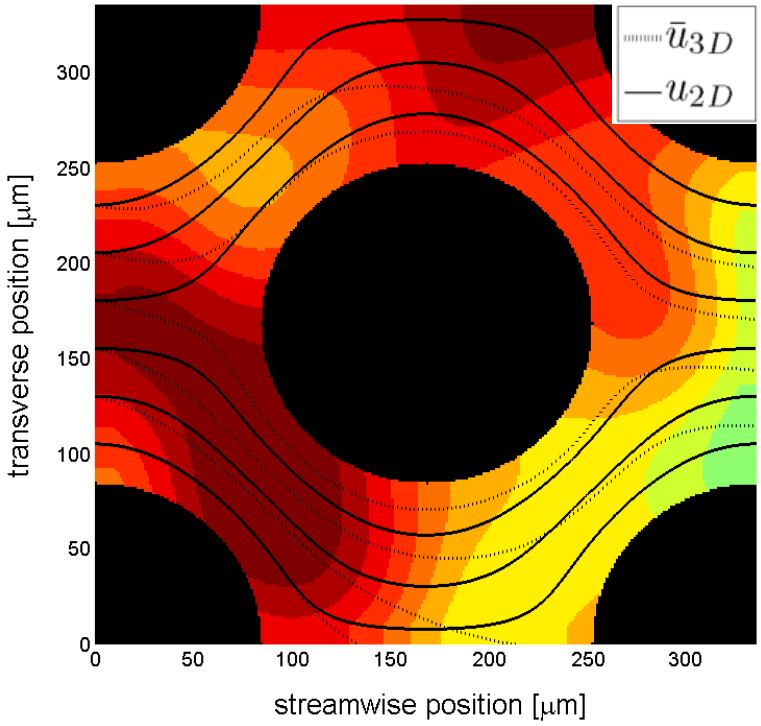

Figure 32: Streamlines in the unit cell with random depth and $\boldsymbol{h(x, y)}$. $\boldsymbol{u_{2D}(x, y)}$ is solved without including viscous drag from the top and bottom MFD surfaces.

For the maximum and average value of the transverse component, the least absolute error comes from including viscous drag and scaling $\boldsymbol{u}_{\boldsymbol{2D}}(x, y)$. Although errors in the streamwise component are greater with the addition of viscous drag, the absolute error is still relatively small at less than 2%. On the other hand, the addition of viscous drag reduces error in the transverse component by more than 10%. These results suggest the optimal approach may be to include both scaling and viscous drag. At least in this geometry, scaling reduces both streamwise and transverse error. Incorporating viscous drag further reduce transverse error, at the expense of adding some streamwise error.

CHAPTER 5: DISCUSSION

Ten test geometries have been studied to determine if a 2D, depth-averaged LBM can successfully approximate the depth-averaged results of a 3D LBM to reduce the computational cost of reactive transport models in MFDs. Existing work in the literature has successfully implemented this approximation for the case of a constant depth MFD. The method proposed in this thesis extends that work to cases of spatially-variable depth.

The first four test geometries were variations of an expanding-contracting channel in which depth varied only in the streamwise direction. These simple geometries discerned the relative error caused by rapid and asymmetric depth variation, finding the former to be more significant than the latter. Other test geometries were more complex and included flow around cylinder pillars and through a channel with randomly-generated depth. The more complex flows in these geometries resulted in greater discrepancy between the true velocity field and its approximation.

In general, the streamwise component of velocity was approximated more closely than the transverse component. This result can be explained, at least in part, by the scaling procedure implemented to guarantee that velocity fields are compared with equal volumetric flow rate. Scaling was required because we could not determine, a priori, the driving force (pressure gradient) needed in paired 2D and 3D simulations to produce equal flow rate; equal driving force did not produce equal flow rate. Although scaling can be justified for the case of Stokes flow considered in this work, the need to scale limits application of the proposed method to other flows.

The 2D, depth-averaged LBM incorporates viscous drag from the horizontally-oriented top and bottom MFD surfaces by approximating it with an external resistive acceleration. However, the effect of viscous drag from vertically-oriented solid surfaces, such as the sides of cylindrical pillars, is not accounted for. The influence of these surfaces on the velocity field should be studied further to improve accuracy of the 2D approximation.

An additional limitation of the proposed approach is the propagation and increase of error with streamwise length. If streamline separation is an acceptable measure, it seems that in complex and asymmetric geometries errors in the velocity field will increase with streamwise length of the simulation domain. This property is problematic for the accuracy of 2D solute transport and reaction models coupled to the 2D, depth-averaged LBM. Further numerical experiments in larger and more complex domains are needed to discern the severity of this potential limitation.

Based on results in the final and most complex test case, the proposed 2D, depth-averaged approach would not approximate the transport of solutes in a MFD to high accuracy, its primary shortcoming being poor prediction of transverse flow. However, it is expected to be more accurate than existing 2D approaches, because it includes some 3D effects. Including additional 3D effects, such as viscous drag from vertically-oriented surfaces, or utilizing a different LBM body force implementation, may further increase accuracy. Still, it is likely the proposed 2D method will provide a rough approximation of reactive transport in complex, 3D systems. For applications where a rough approximation is sufficient, much computational time can be saved with a 2D method. For applications requiring higher accuracy, 3D methods should be employed.

BIBLIOGRAPHY

Bhatnagar, P.L., E.P. Gross, and M. Krook. “A Model for Collision Processes in Gases. I. Small Amplitude Processes in Charged and Neutral One-Component Systems.” *Physical Review* 94, no. 3 (1954).

Boek, E.S. and M. Venturoli. “Lattice-Boltzmann studies of fluid flow in porous media with realistic rock geometries.” *Computers and Mathematics with Applications* 59 (2010): 2305 – 2314.

Flekkoy, E.G., U. Oxaal, J. Feder, and T. Jossang. “Hydrodynamic Dispersion at Stagnation Points: Simulations and Experiments.” *Physical Review E* 52, no. 5 (1995).

Guo, Z., C. Zheng, and B. Shi. “Discrete Lattice Effects on the Forcing Term in the Lattice Boltzmann Method.” *Physical Review E* 65 (2002).

He, X. and L.S. Luo. “Lattice Boltzmann model for the incompressible Navier-Stokes equations.” *Journal of Statistical Physics* 88, (1997).

Interactive Models for Groundwater Flow and Solute Transport. Last modified April 2014, http://hydrolab.illinois.edu/gw_applets//?q=gw_applets/.

Latt, J. “Choice of units in lattice Boltzmann simulations.” Freely available online at http://lbmethod.org/_media/howtos:lbunits.pdf. (2008).

Luo, Li-Shi. “Theory of the Lattice Boltzmann Method: Lattice Boltzmann Models for Nonideal Gases.” *Physical Review E* 62, no. 4 (2000): 4982.

Mohamad, A.A. and A. Kuzmin. “A Critical Evaluation of Force Term in Lattice Boltzmann Method, Natural Convection Problem.” *International Journal of Heat and Mass Transfer* 53 (2010).

Nambi, I.M., C.J. Werth, R.A. Sanford, and A.J. Valocchi. 2003. “Pore-Scale Analysis of Anaerobic Halorespiring Bacterial Growth Along the Transverse Mixing Zone of an Etched Silicon Pore Network.” *Environ. Sci. Technol.* 37: 5617–5624.

Succi, S. *The Lattice Boltzmann Equation for Fluid Dynamics and Beyond*. Oxford: Clarendon Press, 2001.

Sukop, M.C. and D.T. Thorne, Jr. *Lattice Boltzmann Modeling: An Introduction for Geoscientists and Engineers*. Springer, 2007.

Venturoli, M. and E.S. Boek. “Two-dimensional lattice-Boltzmann Simulations of Single Phase Flow in a Pseudo Two-dimensional Micromodel.” *Physica A: Statistical Mechanics and Its Applications* 362, no. 1 (2006): 23–29.

White, F.M. *Viscous Fluid Flow*. 2nd ed. McGraw-Hill, Inc., 1991.

Willingham, T., C. Zhang, C.J. Werth, A.J. Valocchi, M. Oostrom, and T.W. Wietsma. 2010. “Using Dispersivity Values to Quantify the Effects of Pore-scale Flow Focusing on Enhanced Reaction Along a Transverse Mixing Zone.” *Advances in Water Resources* 33: 525–535.

Willingham, T. W., C. J. Werth, and A. J. Valocchi. “Evaluation of the effects of porous media structure on mixing-controlled reactions using pore-scale modeling and micromodel experiments.” *Environmental Science & Technology* 42, (2008): 3185-3193.

Yoon, H., A. J. Valocchi, C. J. Werth, and T. Dewers. “Pore-scale simulation of mixing-induced calcium carbonate precipitation and dissolution in a microfluidic pore network.” *Water Resources Research* 48, (2012).

Zhang, C., K. Dehoff, T. Wietsma, A. Valocchi, B. Fouke, and C. Werth. “Pore-Scale Study of Transverse Mixing Induced $CaCO_3$ Precipitation and Permeability Reduction in a Model Subsurface Sedimentary System.” *Environ. Sci. Technol.* 44 (2010): 7833–7838.

Zou, Q. and X. He. “On Pressure and Velocity Boundary Conditions for the Lattice Boltzmann BGK Model.” *Physics of Fluids* 9, no. 6 (1997).

APPENDIX A: SUMMARY OF ANALYTICAL SOLUTIONS FOR OPEN, RECTANGULAR CHANNEL FLOWS

Flow in a 3D channel with rectangular cross section

The steady-state 3D velocity profile, defined over a rectangular cross section such that $-w/2 \leq y \leq w/2$ and $-h/2 \leq z \leq h/2$, is reported in Eq. 14 (White 1991). dP/dx is the pressure gradient in the streamwise direction, h is the constant channel depth, w is the constant channel width, μ is the fluid dynamic viscosity, y is the transverse spatial coordinate, and z is the vertical spatial coordinate.

$$u_{3D,x}(y,z) = \frac{4w^2}{\mu\pi^3}\left(-\frac{dP}{dx}\right)\sum_{i=1,3,\ldots}^{\infty}(-1)^{(i-1)/2}\left[1-\frac{\cosh(i\pi z/w)}{\cosh(i\pi h/2w)}\right]\frac{\cos(i\pi y/w)}{i^3} \qquad \text{Eq. 14}$$

Integrating the velocity profile over the cross section yields the volumetric flow rate (Q), reported in Eq. 15 (White 1991). Note the flow rate is equivalent to the average streamwise velocity (u_{ave}) multiplied by the cross-sectional area ($A = wh$).

$$Q_{3D} = u_{ave}A = \frac{hw^3}{12\mu}\left(-\frac{dP}{dx}\right)\left[1-\frac{192w}{\pi^5 h}\sum_{i=1,3,\ldots}^{\infty}\frac{\tanh(i\pi h/2w)}{i^5}\right] \qquad \text{Eq. 15}$$

Flow in a 2D rectangular channel (Poiseuille flow)

The Poiseuille velocity profile is reported in Eq. 16 and Eq. 17, with all parameters previously defined. Eq. 16 defines the profile in a vertical ($x-z$) plane, with depth h and spatial coordinate z. Eq. 17 defines the profile in a horizontal ($x-y$) plane, with width w and spatial coordinate y. In both cases, no-slip boundaries are assumed. In Figure 4 the Poiseuille profile was applied in the horizontal plane, while in Figure 7 it is applied in the vertical plane.

$$u_{2D}(z) = \left(-\frac{dP}{dx}\right)\left(\frac{h^2}{8\mu}\right)\left(1-\frac{4z^2}{h^2}\right) \qquad \text{Eq. 16}$$

$$u_{2D}(y) = \left(-\frac{dP}{dx}\right)\left(\frac{w^2}{8\mu}\right)\left(1 - \frac{4y^2}{w^2}\right) \qquad \text{Eq. 17}$$

Flow in a 2D rectangular channel, with viscous drag from top and bottom surfaces

The analytical velocity profile in a 2D channel with viscous drag from top and bottom implicit surfaces is derived from the governing ordinary differential equation in Appendix B. The solution is reported in Eq. 18. Note this velocity profile applies only for fully-developed flow in the horizontal $(x - y)$ plane.

$$u_{2D}(y) = \left(\frac{h^2}{12\mu}\frac{dP}{dx}\right)\left[\frac{e^{k_1 y} + e^{-k_1 y}}{e^{k_2} + e^{-k_2}} - 1\right] \qquad \text{Eq. 18}$$

$$k_1 = \frac{2\sqrt{3}}{h} \qquad\qquad k_2 = \frac{k_1 w}{2}$$

APPENDIX B: DERIVATION OF THE 2D ANALYTICAL VELOCITY PROFILE WITH VISCOUS DRAG

The Stokes equation, with acceleration due to viscous drag from the implicit top and bottom surfaces:

$$0 = \mu\nabla^2\boldsymbol{u} - \nabla P - \frac{12\mu}{h^2}\boldsymbol{u}$$

If $\boldsymbol{u}$ is taken to represent fluid velocity in a 2D channel of constant width, the velocity has only one non-zero component. The one-dimensional velocity profile is denoted $u(y)$ such that $-w/2 \leq y \leq w/2$. Because $u(y)$ is a function of only one spatial variable and the pressure gradient is constant in the flow direction, the vector equation reduces to a scalar equation.

$$0 = \mu\frac{d^2u}{dy^2} - \frac{12\mu}{h^2}u - \frac{dP}{dx}$$

The equation above is a second-order, nonhomogeneous, linear ordinary differential equation. Its solution is the sum of a solution to the corresponding homogeneous equation and a particular solution to the nonhomogeneous equation. The corresponding homogeneous equation is shown below.

$$0 = \mu\frac{d^2u}{dy^2} - \frac{12\mu}{h^2}u$$

To solve it, assume u is an exponential function, $u = e^{k_1 y}$, where k_1 is an unknown constant to be determined. Then the second derivative of u with respect to y equals $k_1^2 e^{k_1 y}$. Substituting these expressions in the equation above yields:

$$0 = \mu e^{k_1 y}\left(k_1^2 - \frac{12}{h^2}\right)$$

The above equation may be divided by the leading factor because this quantity never equals zero. Remaining is a quadratic equation in k_1 with solution:

$$k_1 = \frac{2\sqrt{3}}{h}$$

The homogeneous solution, u_h, can be written as a linear combination of two exponential functions with unknown coefficients A and B.

$$u_h = Ae^{k_1 y} + Be^{-k_1 y}$$

A particular solution, u_p is determined by inspection. Note the governing equation is made nonhomogeneous by a constant, the pressure gradient. If u_p is itself a constant, then its second derivative will equal zero and the second term above may cancel the pressure gradient if chosen appropriately. The following particular solution satisfies the nonhomogeneous differential equation.

$$u_p = -\frac{h^2}{12\mu}\frac{dP}{dx} = -Z$$

Therefore, the solution u is given by:

$$u = u_h + u_p = Ae^{k_1 y} + Be^{-k_1 y} - Z$$

The constants A and B are selected to satisfy the no-slip boundary conditions $u(\pm w/2) = 0$. These conditions lead to the following system of equations.

$$u(-w/2) = Ae^{-k_1 w/2} + Be^{k_1 w/2} - Z = 0$$
$$u(w/2) = Ae^{k_1 w/2} + Be^{-k_1 w/2} - Z = 0$$

Consistency of these two equations requires $A = B$. Making this substitution in the first equation and solving for A yields:

$$A = B = \frac{Z}{e^{k_1 w/2} + e^{-k_1 w/2}}$$

Letting $k_2 = k_1 w/2$, the 2D velocity profile may be written as below.

$$u(y) = \left(\frac{h^2}{12\mu}\frac{dP}{dx}\right)\left[\frac{e^{k_1 y} + e^{-k_1 y}}{e^{k_2} + e^{-k_2}} - 1\right]$$

APPENDIX C: INTEGRATION OF THE 2D ANALYTICAL VELOCITY PROFILE WITH VISCOUS DRAG

The velocity profile derived in Appendix B is reported below.

$$u(y) = \left(\frac{h^2}{12\mu}\frac{dP}{dx}\right)\left[\frac{e^{k_1 y} + e^{-k_1 y}}{e^{k_2} + e^{-k_2}} - 1\right]$$

$$k_1 = \frac{2\sqrt{3}}{h} \qquad k_2 = \frac{k_1 w}{2}$$

The velocity profile is width-averaged to yield the average value u_{ave}. The pressure gradient is then expressed as a function of u_{ave}.

$$\frac{1}{w}\int_{-w/2}^{w/2} u(y)\,dy = \left(\frac{h^2}{12w\mu}\frac{dP}{dx}\right)\int_{-w/2}^{w/2}\left[\frac{e^{k_1 y} + e^{-k_1 y}}{e^{k_2} + e^{-k_2}} - 1\right]dy$$

$$u_{ave} = \left(\frac{h^2}{12w\mu}\frac{dP}{dx}\right)\left[\left(e^{k_2} + e^{-k_2}\right)^{-1}\int_{-w/2}^{w/2}\left(e^{k_1 y} + e^{-k_1 y}\right)dy - \int_{-w/2}^{w/2} dy\right]$$

$$= \left(\frac{h^2}{12w\mu}\frac{dP}{dx}\right)\left[\frac{1}{k_1}\left(e^{k_2} + e^{-k_2}\right)^{-1}\left[e^{k_1 y} - e^{-k_1 y}\right]_{-w/2}^{w/2} - [y]_{-w/2}^{w/2}\right]$$

$$= \left(\frac{h^2}{12w\mu}\frac{dP}{dx}\right)\left[\frac{2\left(e^{k_2} - e^{-k_2}\right)}{k_1\left(e^{k_2} + e^{-k_2}\right)} - w\right]$$

$$= \left(\frac{h^2}{12w\mu}\frac{dP}{dx}\right)\left[\frac{2\left(e^{k_2} - e^{-k_2}\right) - wk_1\left(e^{k_2} + e^{-k_2}\right)}{k_1\left(e^{k_2} + e^{-k_2}\right)}\right]$$

$$= \left(\frac{h^2}{12w\mu}\frac{dP}{dx}\right)\left[\frac{(2-wk_1)e^{k_2}-(2+wk_1)e^{-k_2}}{k_1(e^{k_2}+e^{-k_2})}\right]$$

$$= \left(\frac{h^2}{12w\mu}\frac{dP}{dx}\right)\left[\frac{(2-2k_2)e^{k_2}-(2+2k_2)e^{-k_2}}{k_1(e^{k_2}+e^{-k_2})}\right]$$

$$= \left(\frac{h^2}{12w\mu}\frac{dP}{dx}\right)\left(\frac{2}{k_1}\right)\left[\frac{(1-k_2)e^{k_2}-(1+k_2)e^{-k_2}}{e^{k_2}+e^{-k_2}}\right]$$

$$= \left(\frac{h^2}{6k_1w\mu}\frac{dP}{dx}\right)\left[\frac{(1-k_2)e^{k_2}-(1+k_2)e^{-k_2}}{e^{k_2}+e^{-k_2}}\right]$$

$$\frac{dP}{dx} = \frac{6k_1wu_{ave}\mu}{h^2}\left[\frac{(1-k_2)e^{k_2}-(1+k_2)e^{-k_2}}{e^{k_2}+e^{-k_2}}\right]^{-1}$$